Terahertz wave generation based on semiconductor photonic integrated devices

キム, ヨンジン

Terahertz Wave Generation based on Semiconductor Photonic Integrated Devices

Department of Electrical and Electronic Engineering
Graduate School of Information Science and Electrical Engineering

Kyushu University

Younjin Kim

2021

Abstract

Data rate of wireless communication has been gradually increased year after year. The use of wider bandwidth in communication system can be one of the solutions for overcoming the demand. Terahertz wave which is defined as frequency range from 100 GHz to 10 THz is eligible for applying to next generation communication. For photonic terahertz wave generation, photomixing technique makes terahertz wave by taking frequency difference between two continuous lightwaves from two laser sources. The uni-traveling carrier photodiode (UTC-PD) has been used as a photomixer. The UTC-PD has high speed characteristics from electrons as active carrier. In spite of the merits of the UTC-PD, the UTC-PD has output saturation current occurred from decreased electric field, the problem of power saturation at the UTC-PD results in low power should be solved for higher power. Moreover, at high frequency band such as terahertz wave, power loss from the absorption into the air can be also dominant reason to get higher power. The arrayed configuration combining output power between the arrayed photomixers is proposed for power enhancement. The arrayed light sources which can provide same sets of dual wavelengths that can generate terahertz wave with each photomixers are required for practical use without fiber-optics components. On the basis of optical waveguide design, the arrayed photomixers consist of multimode interference (MMI) splitters, bending waveguides and evanescently coupled UTC-PDs with integrated antennas. Distributed feedback (DFB) lasers, MMIs as optical coupler and splitters and semiconductor optical amplifiers (SOAs) should be integrated for the arrayed light sources. The two integrated devices are designed as terahertz wave generator and investigated for terahertz wave generation.

In Chapter 1, the research background for photonics integrated devices is introduced. The configuration of proposed arrayed devices is explained.

In Chapter 2, basic theories for designing each component of the devices are explained.

In Chapter 3, each properties of designed components for the arrayed photomixers are described. We obtain total efficiency at the optimized structure of the device. Finally, the measured responsivity of the integrated device is explained.

In Chapter 4, design of MMIs and bending waveguides for the arrayed light sources is introduced. The measured power uniformity of each SOA output at the device is explained.

In Chapter 5, 600 GHz beam forming at proposed terahertz wave generator combining the arrayed light sources and the arrayed photomixers is explained.

In Chapter 6, this thesis is summarized with outlook.

Table of Contents

1. Introduction 1

1.1 Terahertz wave for wireless communication 1

1.2 Photomixing technique for photonic THz-wave generation 4

1.3 Power enhancement by arrayed configuration 7

1.4 Proposed terahertz wave generator 9

1.5 Topics of this thesis 11

References 12

2. Theory for device design 17

2.1 Optical Waveguide 17

2.2 Multimode interference 25

2.3 Evanescent coupling for design of UTC-PD 30

2.4 Phased array antenna 32

2.5 Conclusions 37

References 38

3. Arrayed photomixers 41

3.1 Waveguide for photomixer design 41

3.2 Design of bending waveguide 47

3.3 Multimode interference splitter 52

3.4 Evanescently coupled photodiode 56

3.5 Performance of arrayed photomixers 62

3.6 Conclusions 66

References 67

4. Arrayed light sources 69

4.1 Design of multimode interference splitter and bending waveguide 69

4.2 Performance of arrayed light sources 75

4.3 Conclusions 78

References 79

5. Demonstration of terahertz wave generation 81

5.1 Experimental configuration for terahertz power detection 81

5.2 Beamforming at 600 GHz using integrated devices 83

5.3 Conclusions 85

References 86

6. Conclusion and Outlook 87

6.1 Conclusion 87

6.2 Outlook 90

List of abbreviations 91

Acknowledgement 93

1. Introduction

1.1 Terahertz wave for wireless communication

Recent communication has been an essential element in rapidly growing society and supports a various pattern of communication with development of electronic devices. Data rate of wireless communication has been continuously increasing with such a trend year after year. The expectation of the data rates of around 100 Gbit/s near 2020 was reported [1-2]. Recently, the stage of commercialized communication has been reached to the fifth generation (5G) wireless communication at frequency band of millimeter wave [3]. Some technologies have been studied for the wide-band communication [4]. To keep up with increasing data rate, the use of wider bandwidth in communication system can be one of the solutions for overcoming the demand of high data rate. However, an available bandwidth is obtained by approximately 10 % of operating frequency [5]. As for the promising carrier frequency in the near future beyond 5 G, terahertz wave which is defined as frequency range from 100 GHz to 10 THz has been investigated so that it can be applied to next generation communication [6-7]. The terahertz wave region which is so-called terahertz gap as shown in **Fig. 1.1** indicates the range between a low frequency band radiated by oscillating circuits using high speed transistors and a high frequency band generated by semiconductor lasers using optical fibers [8]. Each frequency band is separately existed and not overlapped. But it is difficult to generate by each electronics and photonics approach. **Figure 1.1** describes the terahertz gap and THz sources with generated THz power depending on the frequency range of terahertz wave [9]. Since the terahertz wave has beneficial characteristics coming from penetration and straightness, recently it has been developed in various research fields such as biology, medical and pharmaceutical sciences, security, information and communication technologies as well as astronomy which

has been studied long earlier than other fields [8-10].

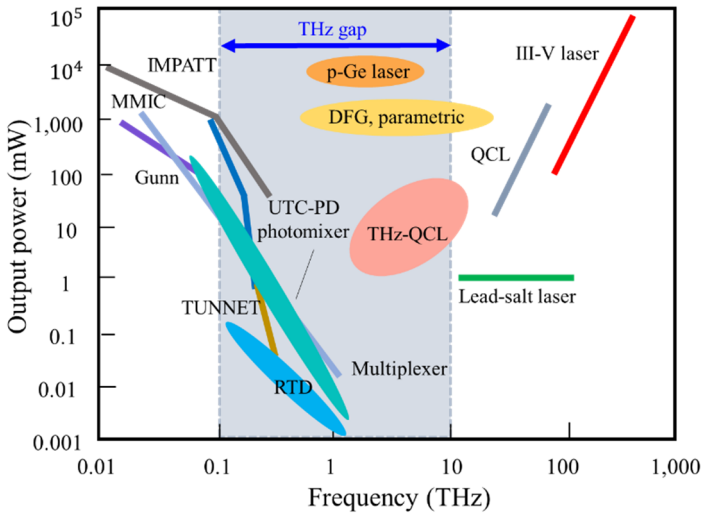

Fig. 1.1 Output power as a function of THz frequency [9].

On the other hand, the high frequency band such as the terahertz wave has drawbacks of a low power from the output limit of THz sources itself [11] and power attenuation from the absorption into the air [12]. The terahertz wave is generated by either electronics or photonics according to the same configuration as referred above. The THz sources of solid-state electronic devices which can be divided by the two categories have been developed**.**

First, there have been many researches using the THz sources based on electronics approach. The sources are resonant tunneling diode (RTD) [13-14], monolithic microwave integrated circuit (MMIC) [15], impact ionization avalanche transit-time (IMPATT) diode [16], Gunn diode [17], tunneling transit-time (TUNNETT) diode [18-19], Si-CMOS device [20], etc. Meanwhile, in photonics approach, there are the sources such as THz quantum cascade laser (THz-QCL) [21-23], p-Ge laser [24], uni-traveling carrier photodiode (UTC-PD) [25] as photomixer, etc. As for the two approaches applied to wireless transmission system using the THz-wave, the difference between them has been reported in the relation between achieved

data rate and carrier frequency [26]. In this report, the photonics-based method attained a higher data rate at the carrier frequency range of 200-400 GHz even though that of the electronics-based almost occupied at 100-150 GHz carrier frequency. The transmitter based on the two approaches was described in **Fig. 1.2**.

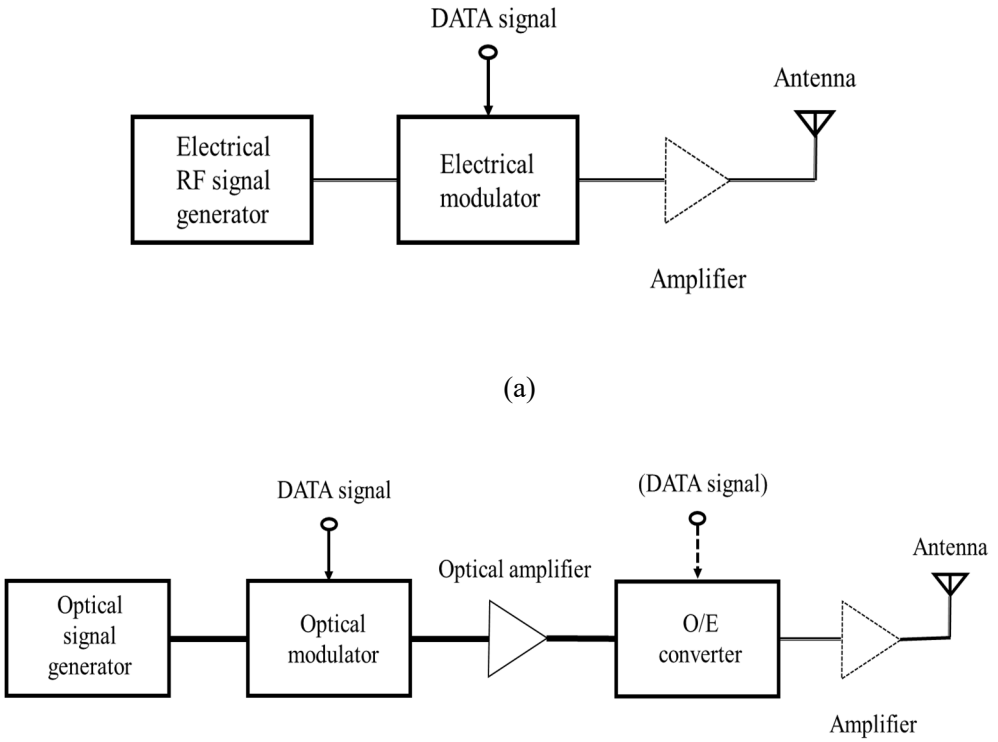

Fig. 1.2 Each THz transmitter [26]. (a) Electronics-based. (b) Photonics-based.

The photonics-based THz transmitter as shown in **Fig. 1.2 (b)** uses fiber-optic configuration which results in a remarkable feature that the seamless connections between fiber-optic and wireless communication networks are available with respect to data rates and the format of modulation [26] even though the electronics-based transmitter as shown in **Fig. 1.2 (a)** has been also widely used in the wireless transmission. However, the transmission above the frequency of 500 GHz at both approaches should be improved due to a low data rate caused by

the insufficient power from the transmitter [26]. Therefore, the enhancement of output power at the transmitter is needed. In terms of the data rate at THz frequency, the development of THz sources and related technologies has been an issue. We chose the photonics-based terahertz generation method for our research.

1.2 Photomixing technique for photonic THz-wave generation

For the photonics-based THz-wave generation, photomixing technique is used at the generation of optical signals at THz frequency band and making the THz frequency based on the heterodyne conversion [27]. The merit of the photomixing is that the wide range of frequency tuning is available [26], [28]. The photomixing makes the terahertz wave by taking frequency difference between two continuous lightwaves of f_1 and f_2 from two laser sources. In the photomixing process, the two lightwaves are introduced into photomixer such as photoconductor and photodiodes. The optical-to-electrical conversion at the photomixer leads to the THz-wave generation [29-32]. **Figure 1.3** shows terahertz wave generation mechanism by the photomixing. The two lightwaves formed from two lasers are coupled at an optical coupler. The coupled light is converted to terahertz wave and the terahertz wave is detected at a photomixer. The generated terahertz wave after the photomixing has the frequency and the phase which indicates frequency difference of $f_1 - f_2$ and phase difference of $\varphi_1 - \varphi_2$ between the original two lightwaves, respectively. To make an effective photomixing, there is a significance of stabilized features at frequency and phase as well as polarization of the two lightwaves [33].

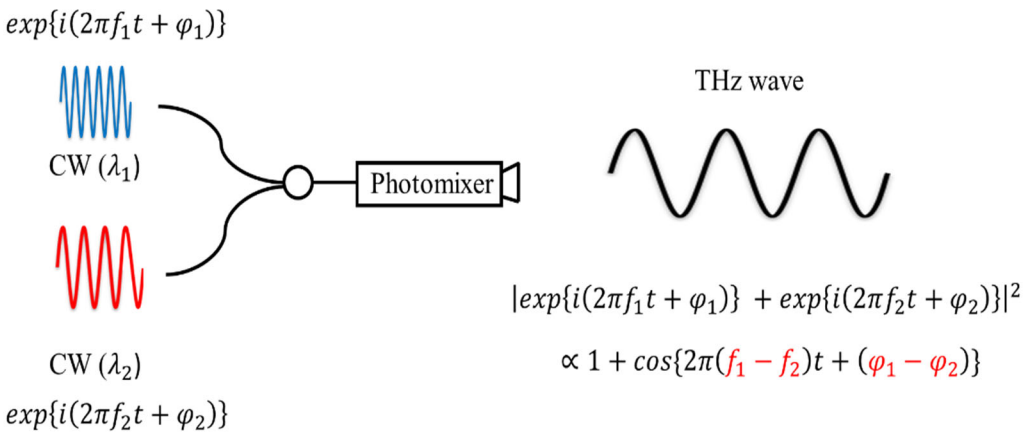

Fig. 1.3 Schematic of photomixing technique.

The UTC-PD is used as one of the photomixers because of its high speed response. There have been also other merits of obtaining a higher operation current and the use of a lower operation voltage. On the other hand, holes with low velocity contribute to the performance of the pin-photodiode (pin-PD) while this PD operates by the characteristics of both holes and electrons as carriers as shown in **Fig. 1.4 (a)** [25],[34]. The high speed characteristic of the UTC-PD comes from the phenomenon that the electrons diffused from the p-doped photoabsorption layer travel into the carrier collection layer with high velocity as shown in **Fig. 1.4 (b)**. In spite of the merits of the UTC-PD compared to the conventional pin-PD, the UTC-PD has also output saturation current occurred from decreased electric field due to excitation of photogenerated carriers as shown in **Fig. 1.5**. The thermal effects are involved in the saturation characteristic, the problem of power saturation at the UTC-PD, which results in low power can be one of the obstacles for obtaining a high power [34]. Thus, the methods for power combination are needed.

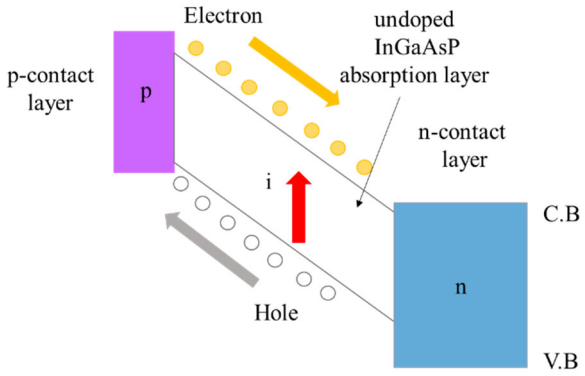

(a)

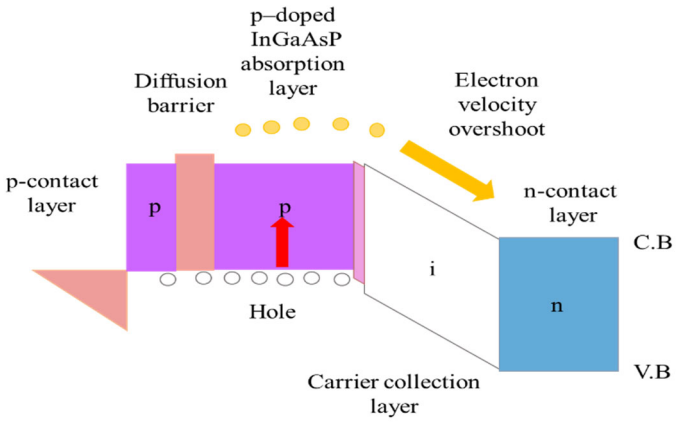

(b)

Fig. 1.4 Band diagram [25]. (a) Conventional pin-PD. (b) UTC-PD.

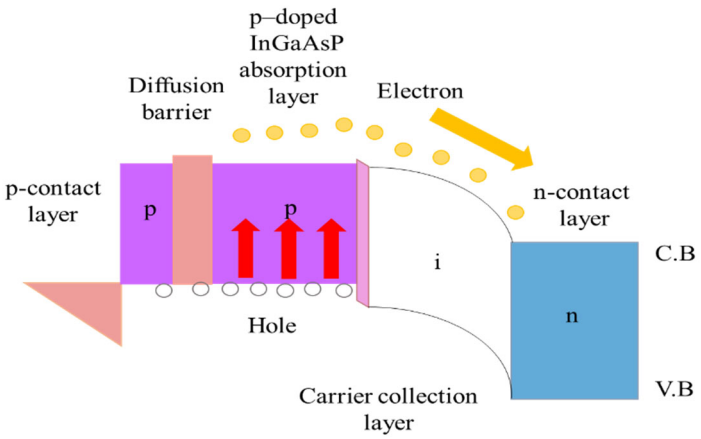

Fig. 1.5 Band diagram of UTC-PD in power saturation [25].

Figure 1.6 shows measured terahertz power at single UTC-PD and the saturation characteristic at a certain point with increasing optical input power at the condition of 300 GHz frequency operation and -1.5 V bias. Due to the absorption loss as referred in Chapter 1.1, the output power should be improved by arrayed UTC-PDs.

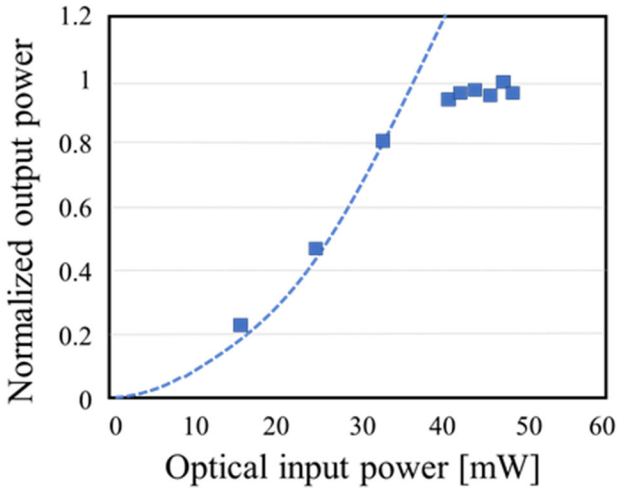

Fig. 1.6 Measured power saturation at single UTC-PD.

1.3 Power enhancement by arrayed configuration

The arrayed configuration combining output power between the arrayed UTC-PDs can be a solution for power enhancement. The configuration aims to combine simultaneously each radiated THz power in the air after THz-wave generation at each UTC-PD and THz-wave radiation by antennas. There are two possible ways for feeding the signal to each antenna. One is electrical feeding lines between UTC-PDs and antennas, and another way is optical feeding lines or waveguides between optical splitter outputs and UTC-PDs. The distance between the UTC-PD and the antenna should be short or they are directly connected so that the electrical signal loss can be reduced as small as possible. We design the structure of closely integrated

UTC-PD and antenna. For the arrayed device, a monolithic integration of optics components designed using semiconductor, which is called photonic integrated circuits (PICs) [35] is needed. Based on the PICs, the research of the UTC-PD which is operated at photomixing system has been investigated [36]. Due to the necessities of the power combination at the arrayed UTC-PDs, the development of monolithically integrated device has been studied. The combined power more than 1mW using two arrayed UTC-PDs for 300 GHz-wave was demonstrated [37]. Because of the effectiveness of arrayed configuration to achieve a high power at terahertz frequency, we propose arrayed UTC-PDs for 600 GHz-wave generation, which can obtain more combined power. The conceptual configuration of the arrayed device is shown as **Fig. 1.7**. The optical waveguide has an important role in feeding optical power from the light sources into each UTC-PD. The radiated terahertz power at each antenna is combined by array factor.

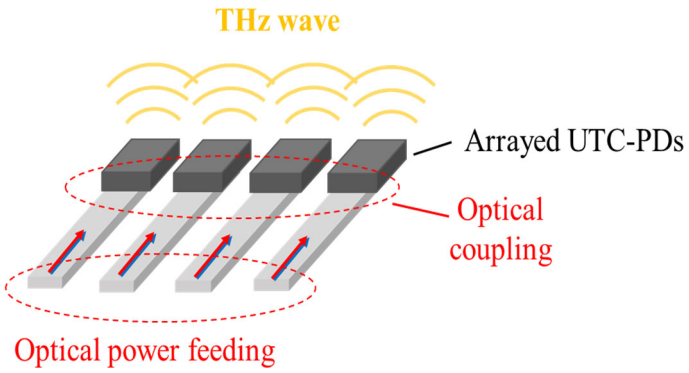

Fig. 1.7 Configuration of arrayed UTC-PDs with optical waveguide.

Meanwhile, a fiber-based configuration that two lightwaves were lased by two lasers, coupled by a fiber coupler and divided into arrayed outputs by fiber splitters was used in the previous demonstration of 600 GHz [38] or 700 GHz [39] wave generation. Moreover, an optical delay line was used at each path to achieve terahertz wave phase matching for in-phase combination.

Although the fiber-based configuration has merits for such a feasibility demonstration, a complexity in the system for the measurement of the terahertz wave remains. Therefore, one way to improve this complexity is a monolithically integrated light source which realizes a single module by integrating the light sources and the UTC-PDs. The basic configuration of the module has been reported in [40] as a part of two-channel THz-wave wireless transmitter with two arrayed UTC-PDs for up to 100 GHz-wave. We aim to make more arrayed UTC-PDs for higher THz power by power combination at our targeting device. We also suggest arrayed UTC-PDs integrated with antennas so that each integrated antenna radiates terahertz wave into the air without outer antenna components. Along with the arrayed UTC-PDs, the arrayed light sources to provide same sets of dual wavelengths that can generate terahertz wave with each arrayed UTC-PDs are proposed as shown in **Fig.1.8.**

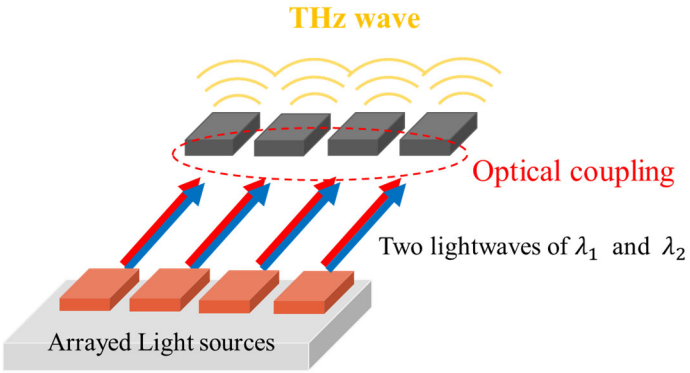

Fig. 1.8 Configuration of arrayed light sources.

1.4 Proposed terahertz wave generator

Our proposed conceptual configuration of the two integrated devices is shown in **Fig. 1.9**. The entire structure describes the proposed terahertz wave generator consisting of the arrayed

light sources and the arrayed UTC-PDs. Two lightwaves from two lasers at the arrayed light sources are distributed into each output for coupling between each output at the sources and the arrayed UTC-PDs. Each UTC-PD generates terahertz current and terahertz wave is radiated by antennas integrated with the UTC-PD. Total path lengths from the lasers to the antennas are required to be designed the same so that the radiated terahertz waves are combined in a same phase. The proposed generator has advantages of compactness, and direct coupling between the output of light source and each UTC-PD without fiber-optics and an additional component. Furthermore, the temperature controller for the lasers is integrated in the section of the light sources. This brings the easiness that the temperature of both lasers can be controlled all at once and a low power consumption while two solitary lasers need each temperature controller. On the other hand, the generator may have a problem of expected low power caused by sensitiveness of the optical coupling with the difficulties on optical alignment.

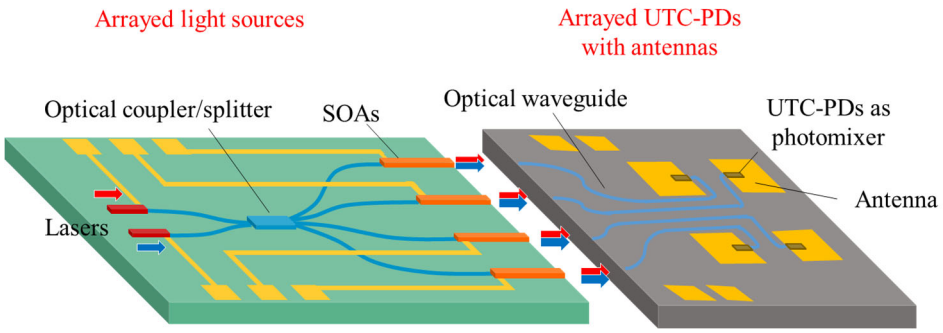

Fig. 1.9 Conceptual configuration of proposed terahertz wave generator.

For the terahertz wave generator, we designed the optical waveguides to make each component of the arrayed photomixers and the arrayed light sources using FIMMWAVE by eigen mode expansion (EME) method [41]. The InP/InGaAsP material system [42] was used to design the semiconductor optical devices. First of all, the arrayed photomixers consist of multimode

interference (MMI) splitters, bending waveguides, and the UTC-PDs. Then, the proposed arrayed light sources have two lasers that can generate two continuous lightwaves, MMI splitters and couplers, semiconductor optical amplifiers (SOAs). The detailed structure of the two integrated devices will be explained in Chapter 3 and Chapter 4.

1.5 Topics of this thesis

In Chapter 2, basic theories for design of the photonic integrated devices are explained. Optical waveguide design of each component for the arrayed photomixers is introduced and the performance of the fabricated device is discussed in Chapter 3. In Chapter 4, the waveguide design of each component for the arrayed light sources is described and the performance of the fabricated device is discussed. Terahertz wave generation between the two photonic integrated devices is demonstrated in Chapter 5. Finally, we conclude this thesis in Chapter 6.

References

[1] S. Cherry, “Edholm’s Law of Bandwidth,” IEEE Spectrum, vol. 41, no. 7, pp. 58–60, 2004.

[2] T. Kürner and S. Priebe, “Towards THz communications - status in research, standardization and regulation,” Journal of Infrared, Millimeter, and Terahertz Waves 35 (1), pp. 53-62, 2014.

[3] Y. Niu, Y. Li, D. Jin, L. Su, and A.V. Vasilakos, “A survey of millimeter wave communications (mmWave) for 5G: opportunities and challenges,” Wireless Networks 21(8), pp. 2657-2676, 2015.

[4] C.-X. Wang, F. Haider, X. Gao, X-H. You, Y. Yang, D. Yuan, HM. Aggoune, H. Haas, S. Fletcher, and E. Hepsaydir, “Cellular architecture and key technologies for 5G wireless communication networks,” IEEE Commun. Mag., vol. 52, no. 2, pp. 122-130, Feb. 2014.

[5] K. R. Jha and G. Singh, “Terahertz Planar Antennas for Next Generation Communication,” Springer International Publishing, 2014.

[6] I. F. Akyildiz, J. M. Jornet, and C. Han, “Terahertz band: Next frontier for wireless communications,” Physical communication, vol. 12, pp.16-32, 2014.

[7] T. S. Rappaport, Y. Xing, O. Kanhere, S. Ju, A. Madanayake, S. Mandal, A. Alkhateeb, and G.C. Trichopoulos, “Wireless Communications and Applications Above 100 GHz: Opportunities and Challenges for 6G and Beyond,” IEEE Access, vol.7, pp.78729-78757, 2019.

[8] C. Sirtori, “Bridge for the terahertz gap,” Nature, vol. 417, Issue 6885, pp. 132-133, 2002.

[9] M. Tonouchi, “Cutting-Edge Terahertz Technology,” Nature Photonics, vol. 1, pp. 97-105, 2007.

[10] P. H. Siegel, “Terahertz technology,” IEEE Trans. Microwave Theory Tech, vol. 50, pp. 910–928, Mar. 2002.

[11] G. Chattopadhyay, “Technology, Capabilities, and Performance of Low Power Terahertz Sources,” IEEE Trans. Terahertz Sci. Technol, vol. 1, no. 1, Sep. 2011.

[12] Specific Attenuation Model for Rain for Use in Prediction methods, ITU-R Recommendation P.838-3, 2005.

[13] E. R. Brown, J. R. Sönderström, C. D. Parker, L. J. Mahoney, K. M. Molvar, and T. C. McGill, "Oscillations up to 712 GHz in InAs/AlSb resonant-tunneling diodes," Appl. Phys. Lett. 58, pp.2291-2293, 1991.

[14] T. Maekawa, H. Kanaya, S. Suzuki, and M. Asada, "Oscillation up to 1.92 THz in resonant tunneling diode by reduced conduction loss," Appl. Phys Express, 9, (2), 024101, 2016.

[15] I. Kallfass, I. Dan, S. Rey, P. Harati, J. Antes, A. Tessmann, S. Wagner, M. Kuri, R. Weber, H. Massler, A. Leuther, T. Merkle, and T. Kürner, "Towards MMIC-Based 300GHz Indoor Wireless Communication," IEICE Trans. Electron, vol. E98-C, no.12, Dec. 2015.

[16] A. Acharyya and J. P. Banerjee, "Prospects of IMPATT devices based on wide bandgap semiconductors as potential terahertz sources," Appl. Nanosci. 4 (1), pp.1-14, 2014.

[17] H. Eisele, "480 GHz oscillator with an InP Gunn device," Electron. Lett, vol.46, no.6, pp. 422-423, 2010.

[18] J. Nishizawa and Y. Watanabe, "High frequency properties of avalanching negative resistance diode," Sci. Rep. Res. Inst. Tohoku Univ. 10 (2), pp.91-108, 1958.

[19] J. Nishizawa, P. Plotka, T. Kurabayashi, and H. Makabe, "706-GHz GaAs CW fundamental-mode TUNNETT diodes fabricated with molecular layer epitaxy," phys. stat, sol, (c)5, no.9, pp.2802-2804, 2008.

[20] K. Sengupta and A. Hajimiri, "A 0.28 THz Power-Generation and Beam-Steering Array in CMOS Based on Distributed Active Radiators," IEEE J. Solid-State Circuits, vol. 47, no. 12, Dec. 2012.

[21] J. Faist, F. Capasso, D. L. Sivco, C. Sirtori, A.L. Hutchinson, and A.Y. Cho, "Quantum Cascade Laser," Science 22 vol. 264, Issue 5158, pp. 553-556, Apr. 1994.

[22] R. Köhler, A.Tredicucci, F. Beltram, H.E. Beere, E. H. Linfield, A. G. Davies, D.A. Ritchie, R. Iotti, and F. Rossi, “Terahertz semiconductor heterostructure laser,” Nature 417, pp.156-159, 2002.

[23] H.-W. Hübers, H. Richter, and M. Wienold, “High-resolution terahertz spectroscopy with quantum-cascade lasers,” J. Appl. Physics 125, 151401, 2019.

[24] A. Bergner, U. Heugen, E. Bründermann, G. Schwaab, M. Havenith, D. R. Chamberlin, and E. E. Haller, “New THz laser spectrometer for the study of solutions: THz absorption spectroscopy of water,” Review of Scientific Instruments 76, 063110, 2005.

[25] T. Ishibashi, T. Furuta, H. Fushimi, S. Kodama, H. Ito, T. Nagatsuma, N. Shimizu, and Y. Miyamoto, “ InP/ InGaAs uni-traveling-carrier photodiodes,” IEICE Trans. Electron, vol. E83-C, no. 6, pp. 938-949, Jun. 2000.

[26] T. Nagatsuma and G. Carpintero, “Recent Progress and Future Prospect of Photonics-Enabled Terahertz Communications Research,” IEICE Trans. On Electronics E98-C (12) pp.1060–1070, 2015.

[27] E. R. Brown, F. W. Smith, and K. A. McIntosh, “Coherent millimeter-wave generation by heterodyne conversion in low-temperature-grown GaAs photoconductors,” J. Appl. Phys, vol. 73, no. 3, pp. 1480–1484, 1993.

[28] P. Gu, M. Tani, K. Sakai, and T. Hidaka, “Generation of cw-terahertz radiation using a two-longitudinal-mode laser diode,” Jpn. J. Appl. Phys. vol.37, pp. L976-L978, part2, no.8b, Aug. 1998.

[29] I. S. Gregory, C. Baker, W. R. Tribe, I.V. Bradley, M. J. Evans, E. H. Linfield, A. G. Davies, and M. Missous, “Optimization of Photomixers and Antennas for Continuous-Wave Terahertz Emission,” IEEE J. Quantum electron. vol. 41, no. 5, May. 2005.

[30] T. Nagatsuma, “Terahertz technologies: present and future,” IEICE Electronics Express, vol.8, no.14, pp.1127-1142, 2011.

[31] H.-J. Song and T. Nagatsuma, “Present and future of terahertz communications,” IEEE Trans. Terahertz Science and Technology, 1, pp.256-263, 2011.

[32] S. Preu, G. H. Döhler, S. Malzer, L. J. Wang, and A. C. Gossard, “Tunable, continuous-wave Terahertz photomixer sources, and applications,” J. Appl, Phys, vol. 109, no. 6, 061301, March. 2011.

[33] J. Federici and L. Moeller, “Review of terahertz and subterahertz wireless communications,” J. Appl. Phys, 107, 111101, 2010.

[34] T. Nagatsuma, “Generating millimeter and terahertz waves,” IEEE microwave magazine, vol. 10, no.4, pp.64-74, Jun. 2009.

[35] T. L. Koch and U. Koren, “Semiconductor photonic integrated circuits,” IEEE J. Quantum Electron. vol.27, no.3, pp. 641-653, 1991.

[36] E. Rouvalis, M. Chtioui, M. Tran, F. Lelarge, F. van Dijk, M. J. Fice, C.C. Renaud, G. Carpintero, and A. J. Seeds, “High-speed photodiodes for InP-based photonic integrated circuits,” Opt. Exp, vol. 20, pp. 9172–9177, 2012.

[37] H.-J. Song, K. Ajito, Y. Muramoto, A. Wakatsuki, T. Nagatsuma, and N. Kukutsu, “Uni-travelling-Carrier Photodiode Module Generating 300 GHz Power Greater Than 1 mW,” J. Lightwave Technol, vol.22, no.7, pp.363-365, July. 2012.

[38] Y. Zhou, G. Sakano, Y. Yamanaka, H. Ito, T. Ishibashi, and K. Kato, “600-GHz-Wave Beam steering by Terahertz-Wave Combiner,” Optical Fiber Communication Conference (OFC), M4J.1, 2018.

[39] Y. Zhou, N. Nishiyama, H. Ito, T. Ishibashi, and K. Kato, “700 GHz terahertz wave beam combination by optical phase control,” Jpn. J. App. Phys. 58, SJJE03. 2019.

[40] F. van Dijk, G. Kervella, M. Lamponi, M. Chtioui, F. Lelarge, E. Vinet, Y. Robert, M.J. Fice, C.C.

Renaud, A. Jimenez, and G. Carpintero, “Integrated InP Heterodyne Millimeter Wave Transmitter,” IEEE Photon. Technol. Lett, vol.26, no.10, pp.965–968, 2014.

[41] D.F.G. Gallagher and T.P. Felici, “Eigenmode Expansion Methods for Simulation of Optical Propagation in Photonics - Pros and Cons,” Proc. SPIE, vol.4987, pp.69-82, 2003.

[42] R. E. Nahory, M. A. Pollack, W. D. Johnston, Jr, and R.L. Barns, “Bandgap versus composition and demonstrated of Vegard’s law for $In_{1-x}Ga_xAs_yP_{1-y}$ lattice matched to InP,” Appl. Phys. Lett, vol. 33, no. 7, pp.659-661, Oct. 1978.

2. Theory for device design

2.1 Optical Waveguide

Each component at the proposed integrated two devices is required to be designed using optical waveguide. Planar optical waveguides are the key devices as well as the basic elements to make the integrated optical devices with waveguide mechanism [1-2]. Slab waveguide in the planar waveguide can be used for the design of semiconductor lasers and integrated optical circuits [3]. The optical waveguide consists of the core that is involved in light confinement and the cladding or the substrate as shown in **Fig. 2.1**. The core with a refractive index n_1 has a higher refractive index compared to the cladding with a refractive index n_0 and the substrate with a refractive index n_s. The optical waveguide is analyzed based on the Maxwell's equations [4] and wave equations. The optical modes at the waveguide structure are required to design a low loss waveguide. In this thesis, the optical waveguide is explained by based on the slab waveguide structure [2].

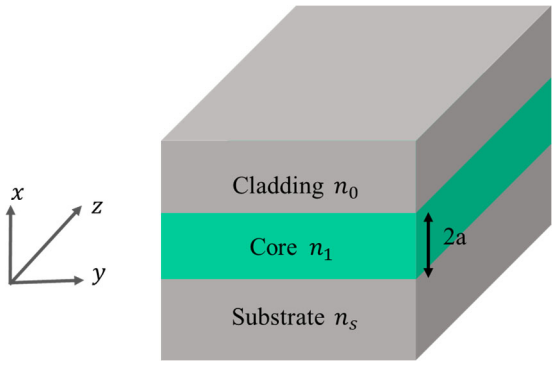

Fig. 2. 1 Structure of slab waveguide [2].

First of all, in Maxwell's equation, the electric field $\tilde{E}$ and the magnetic field $\tilde{H}$ have the relations expressed as **Eq. (2.1.1)** and **Eq. (2.1.2)**.

$$\nabla \times \widetilde{\mathrm{E}} = -\mu_0 \frac{\partial \widetilde{\mathrm{H}}}{\partial t} \quad \textbf{(2.1.1)}$$

$$\nabla \times \widetilde{\mathrm{H}} = \varepsilon_0 n^2 \frac{\partial \widetilde{\mathrm{E}}}{\partial t} \quad \textbf{(2.1.2)}$$

The permittivity of $\varepsilon = \varepsilon_0 n^2$ and the permeability of $\mu = \mu_0$ at the medium are given above in the equations. ω indicates the angular frequency of the sinusoidally varying electromagnetic fields by time. The sinusoidal function of $\widetilde{\mathrm{E}}$ and $\widetilde{\mathrm{H}}$ can be converted into the expression of phasors as **Eq. (2.1.3)** and **Eq. (2.1.4)**

$$\widetilde{\mathrm{E}}(t) = \mathrm{E}(x,y)e^{j(\omega t - \beta Z)} \quad \textbf{(2.1.3)}$$

$$\widetilde{\mathrm{H}}(t) = \mathrm{H}(x,y)e^{j(\omega t - \beta Z)} \quad \textbf{(2.1.4)}$$

Then, **Eq. (2.1.5)** and **Eq. (2.1.6)** are obtained using two equations above**.** The slab waveguides can be analyzed by the following equations.

$$\begin{aligned} \frac{\partial E_Z}{\partial y} + j\beta E_y &= -j\omega\mu_0 H_x \\ -j\beta E_x - \frac{\partial E_Z}{\partial x} &= -j\omega\mu_0 H_y \\ \frac{\partial E_y}{\partial x} - \frac{\partial E_x}{\partial y} &= -j\omega\mu_0 H_z \end{aligned} \quad \textbf{(2.1.5)}$$

$$\begin{aligned} \frac{\partial H_Z}{\partial y} + j\beta H_y &= j\omega\varepsilon_0 n^2 E_x \\ -j\beta H_x - \frac{\partial H_Z}{\partial x} &= j\omega\varepsilon_0 n^2 E_y \\ \frac{\partial H_y}{\partial x} - \frac{\partial H_x}{\partial y} &= j\omega\varepsilon_0 n^2 E_z \end{aligned} \quad \textbf{(2.1.6)}$$

In the slab waveguide, $\frac{\partial \boldsymbol{E}}{\partial y} = 0$ and $\frac{\partial \boldsymbol{H}}{\partial y} = 0$ are placed because y-axis dependency of electromagnetic fields of **E** and **H** does not need to be considered. With **Eq. (2.1.5)** and **Eq.**

(2.1.6), two different electromagnetic modes which are classified as transverse electric (TE) modes and transverse magnetic (TM) modes are obtained. The TE mode satisfies wave equations as **Eq. (2.1.7)** by **Eqs. (2.1.8)-(2.1.10)**.

$$\frac{d^2E_y}{dx^2} + (k^2n^2 - \beta^2)E_y = 0 \quad \textbf{(2.1.7)}$$

$$H_x = -\frac{\beta}{\omega\mu_0}E_y \quad \textbf{(2.1.8)}$$

$$H_z = \frac{j}{\omega\mu_0}\frac{dE_y}{dx} \quad \textbf{(2.1.9)}$$

$$E_x = E_z = H_y = 0 \quad \textbf{(2.1.10)}$$

As represented in **Eq. (2.1.10)**, E_z which is the component of electric field at the z-axis is equal to zero. The tangential components E_y and H_Z have to be continuous at the boundaries of two different media. In the TE mode, the electric field lies in the plane perpendicular to the z-axis while the magnetic field lies in that perpendicular to the z-axis in the TE mode. In the TM mode, the wave equation of **Eq. (2.1.11)** is satisfied from **Eqs. (2.1.12)-(2.1.14)**.

$$\frac{d}{dx}\left(\frac{1}{n^2}\frac{dH_y}{dx}\right) + \left(k^2 - \frac{\beta^2}{n^2}\right)H_y = 0 \quad \textbf{(2.1.11)}$$

$$E_x = \frac{\beta}{\omega\varepsilon_0 n^2}H_y \quad \textbf{(2.1.12)}$$

$$E_z = -\frac{j}{\omega\varepsilon_0 n^2}\frac{dH_y}{dx} \quad \textbf{(2.1.13)}$$

$$E_y = H_x = H_z = 0 \quad \textbf{(2.1.14)}$$

The component of magnetic field at the z-axis H_z is zero as represented in **Eq. (2.1.14)**. According to **Eqs. (2.1.7)-(2.1.10)** or **Eqs. (2.1.11)-(2.1.14)**, each propagation constant and

electromagnetic field at TE and TM modes can be obtained. The dispersion equation as the eigenvalue equation and distributions of the electromagnetic field can be derived from the following calculation method in the slab waveguide with refractive index profile as shown in **Fig. 2.2**. The electromagnetic fields are guided and confined in the core with uniform refractive index profile and exponentially dissipated in the cladding. The distribution of electric field is represented as **Eq. (2.1.15)**. The electric field component E_y has continuity at the boundaries of core-cladding interfaces ($x = \pm a$). Wave numbers of κ, σ, and ξ along the *x*-axis in the core and cladding regions are shown in **Eq. (2.1.16)**.

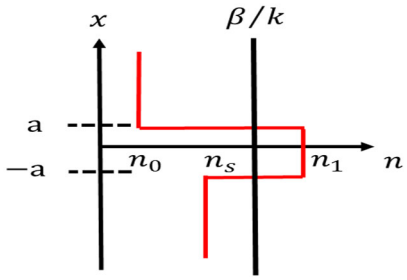

Fig. 2.2 Refractive index profile in slab waveguide [2].

$$\mathrm{E}_y = \begin{cases} A\cos(\kappa a - \varphi)e^{-\sigma(x-a)} & (x > a) \\ A\cos(\kappa a - \varphi) & (-a \le x \le a) \\ A\cos(\kappa a + \varphi)\, e^{\xi(x+a)} & (x < -a) \end{cases} \tag{2.1.15}$$

$$\begin{cases} \kappa = \sqrt{k^2 {n_1}^2 - \beta^2} \\ \sigma = \sqrt{\beta^2 - k^2 n_0^2} \\ \xi = \sqrt{\beta^2 - k^2 n_s^2} \end{cases} \tag{2.1.16}$$

There is another boundary condition which indicates that the magnetic field component H_Z should be continuous at the boundaries. Then, H_Z can be obtained in **Eq. (2.1.9)**. Regardless of the terms independent of *x,* the boundary condition for H_Z is dealt with the continuity

condition of dE_y/dx as expressed in **Eq. (2.1.17)**.

$$\frac{\mathrm{dE}_y}{dx} = \begin{cases} -\sigma A\cos(\kappa a-\varphi)e^{-\sigma(x-a)} & (x>a) \\ -\kappa A\, sin(\kappa a-\varphi) & (-a\le x\le a) \\ \xi A\cos(\kappa a+\varphi)\, e^{\xi(x+a)} & (x<-a) \end{cases} \qquad \textbf{(2.1.17)}$$

Equation (2.1.18) is obtained from the conditions which indicate that dE_y/dx are continuous at $x=\pm a$. **Equations (2.1.19)-(2.1.20)** are also obtained by removing the constant A in condition of **Eq. (2.1.21)**.

$$\begin{cases} \kappa A\sin(\kappa a+\varphi)=\xi A\cos(\kappa a+\varphi) \\ \sigma A\cos(\kappa a-\varphi)=\ \kappa A\sin(\kappa a-\varphi) \end{cases} \qquad \textbf{(2.1.18)}$$

$$\tan(u+\varphi)=\frac{w}{u} \qquad \textbf{(2.1.19)}$$

$$\tan(u-\varphi)=\frac{w'}{u} \qquad \textbf{(2.1.20)}$$

$$\begin{cases} u=\kappa a \\ w=\xi a \\ w'=\ \sigma a \end{cases} \qquad \textbf{(2.1.21)}$$

Finally, the eigenvalue equations as shown in **Eq. (2.1.22)** and **Eq. (2.1.23)** are derived from **Eq. (2.1.19)** and **Eq. (2.1.20)**.

$$\mathrm{u}=\ \frac{m\pi}{2}+\ \frac{1}{2}\tan^{-1}\left(\frac{w}{u}\right)+\frac{1}{2}\tan^{-1}\left(\frac{w\prime}{u}\right) \quad (m=0,1,2,\ldots) \qquad \textbf{(2.1.22)}$$

$$\varphi=\ \frac{m\pi}{2}+\ \frac{1}{2}\tan^{-1}\left(\frac{w}{u}\right)-\frac{1}{2}\tan^{-1}\left(\frac{w'}{u}\right) \qquad \textbf{(2.1.23)}$$

The normalized transverse wavenumbers of *u, w* and w' are not independent. Using **Eq.**

(2.1.16) and **Eq. (2.1.21)**, the three wave numbers have the relationships as shown in **Eqs. (2.1.24)-(2.1.26)**.

$$u^2 + w^2 = \ k^2a^2(n_1^2 - n_s^2) \equiv v^2 \qquad \textbf{(2.1.24)}$$

$$w'=\sqrt{\gamma v^2 + w^2} \qquad \textbf{(2.1.25)}$$

$$\gamma = \frac{n_s^2 - n_0^2}{n_1^2 - n_s^2} \qquad \textbf{(2.1.26)}$$

In the three equations above, *v* indicates the normalized frequency and γ is a criterion of the asymmetry of the cladding refractive indices. The normalized frequency *v* and γ are also determined when the wavelength of the light signal and the geometrical parameters of the waveguide are determined. Therefore, *u, w,* w' and φ are obtained by solving the eigenvalue equations of **Eq. (2.1.22)** and **Eq. (2.1.23)** with the restrictions of **Eqs. (2.1.24)-(2.1.26)**.

In the asymmetrical waveguide ($n_s > n_0$) as expressed in **Fig. 2.2**, the higher refractive index n_s is used as the cladding refractive index for the definition of the normalized frequency *v*. Because the cutoff conditions are determined when the normalized propagation constant β/k corresponds to the higher cladding refractive index. **Equations (2.1.22)**, **(2.1.24)** and **(2.1.25)** indicate the dispersion equations or eigenvalue equations for the TE_m modes. When the wavelength of the light signal and the geometrical parameters of the waveguide are fixed, the normalized frequency *v* and asymmetrical parameter γ are fixed. Consequently, the propagation constant β can be determined from these equations.

By considering **Fig. 2.2** or **Eq. (2.1.15)** and **Eq. (2.1.16)**, the transverse wavenumber κ should be a real number for the main part of the optical field which is confined in the core region. The relation between constants and refractive indices is needed in **Eq. (2.1.27)**.

$$n_s \leq \frac{\beta}{k} \leq n_1 \tag{2.1.27}$$

In **Eq. (2.1.27)**, the normalized propagation constant β/k is a dimensionless value and is a refractive index itself for the plane wave. Thus, it is called the effective index and is generally represented as

$$n_e = \frac{\beta}{k} \tag{2.1.28}$$

On condition of $n_e < n_s$, the electromagnetic field in the cladding becomes oscillatory along the transverse direction. As a result, the field is dissipated as the radiation mode. Since the condition $\beta = kn_s$ indicates the critical condition under which the field is cut off and can be the nonguided mode (radiation mode), the condition is called cutoff condition. A new parameter is introduced as shown in **Eq. (2.1.29)**.

$$b = \frac{n_e^2 - n_s^2}{n_1^2 - n_s^2} \tag{2.1.29}$$

The condition for the guided modes is expressed as $0 \leq b \leq 1$, from **Eq. (2.1.27)** and **Eq. (2.1.28)**. And the cutoff condition expressed as the normalized propagation constant *b* indicates $b = 0$. **Equation (2.1.30)** is obtained by the dispersion **Eq. (2.1.22)** using the normalized frequency *v* and the normalized propagation constant *b*.

$$2v\sqrt{1-b} = m\pi + tan^{-1}\sqrt{\frac{b}{1-b}} + tan^{-1}\sqrt{\frac{b+\gamma}{1-b}} \tag{2.1.30}$$

Equation (2.1.16) can be also expressed as

$$\begin{cases} u = v\sqrt{1-b} \\ w = v\sqrt{b} \\ w' = v\sqrt{b+\gamma} \end{cases} \tag{2.1.31}$$

In case of $n_0 = n_s$ of the symmetrical waveguides, the dispersion **Eq. (2.1.22)** and **Eq. (2.1.23)** are reduced into **Eq. (2.1.32)** and **Eq. (2.1.33)** with $\gamma = 0$.

$$u = \frac{m\pi}{2} + \tan^{-1}\left(\frac{w}{u}\right) \quad \textbf{(2.1.32)}$$

$$\varphi = \frac{m\pi}{2} \quad \textbf{(2.1.33)}$$

Equation (2.1.32) can be represented as **Eq. (2.1.34)** or **Eq. (2.1.35)**.

$$w = u\tan\left(u - \frac{m\pi}{2}\right) \quad \textbf{(2.1.34)}$$

$$v\sqrt{1-b} = \frac{m\pi}{2} + \tan^{-1}\sqrt{\frac{b}{1-b}} \quad \textbf{(2.1.35)}$$

From the analysis above, the mechanism of basic optical waveguide structure was explained. Based on the analysis, we consider the information of polarization of mode, guided mode, radiation mode, confinement of electromagnetic field up to each waveguide structure consisting of cladding, core and substrate.

Then, we use InP/InGaAsP material system to design waveguide structure as referred in Chapter 1.4. For the simulation of each component, the material composition at InGaAsP waveguide core layer is calculated by the relation as expressed in **Eqs. (2.1.36)-(2.1.38)**, where each composition is $In_{1-x}Ga_xAs_yP_{1-y}$ with bandgap wavelength of λ_g and bandgap wavelength of E_g [5-6].

$$E_g \text{ [eV]} = 1.35 - 0.72y + 0.12y^2 \quad \textbf{(2.1.36)}$$

$$\lambda_g \text{ [μm]} = 1.240/E_g \text{ [eV]} \quad \textbf{(2.1.37)}$$

$$x = 0.1894y/(0.4184 - 0.013y) \quad \textbf{(2.1.38)}$$

The material composition is obtained by the relation between several parameters as explained above. The refractive index of the InGaAsP material can be obtained by **Eq. (2.1.39)** when we calculate the other conditions from **Eqs. (2.1.40)-(2.1.43)** [6]**.**

$$n = \left[1 + \frac{E_d}{E_0} + \frac{E_d E^2}{E_0^3} + \frac{\eta E^4}{\pi} ln\left(\frac{2E_0^2 - E_g^2 - E^2}{E_g^2 - E^2}\right)\right]^{1/2} \quad \textbf{(2.1.39)}$$

$$\eta = \pi E_d / 2E_0^3 (E_0^2 - E_g^2) \quad \textbf{(2.1.40)}$$

$$E_0 = 0.595x^2(1 - y) + 1.626xy - 1.891y + 0.524x + 3.391 \quad \textbf{(2.1.41)}$$

$$E_d = (12.36x - 12.71)y + 7.54x + 28.91 \quad \textbf{(2.1.42)}$$

$$E = 1.240/\lambda \quad \textbf{(2.1.43)}$$

Finally, we carefully choose the factors explained in this chapter for design of entire waveguide structure.

2.2 Multimode interference

For coupling and splitting the optical power in the integrated devices, the MMI is used as power coupler and divider. The MMI is operated by the self-imaging principle [7], which has the features of multimode waveguide. It is explained that a reproduced input field profile in single or multiple images is represented at periodic intervals along the direction of the propagation. The MMI structure basically consists of two access waveguides at the beginning

and the end of the MMI, and multimode waveguide in the center of the MMI [7-8]. The central section of the MMI generally accompanies with a large number of modes more than 3. N x M MMI as shown in **Fig. 2.3** indicates the number of N for input waveguides and that of M for output waveguides, respectively.

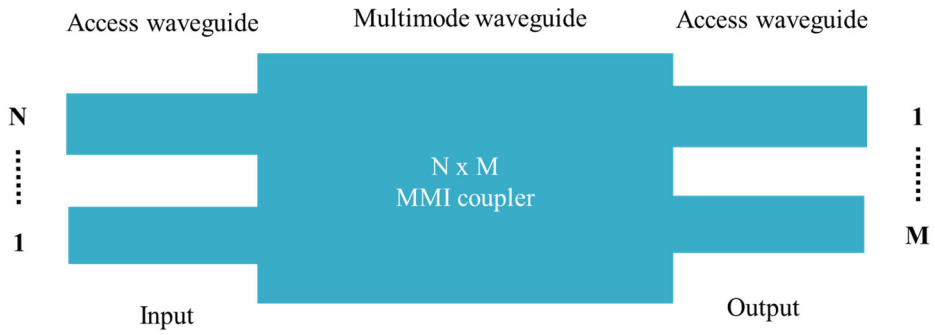

Fig. 2. 3 N x M MMI splitter.

In a step-index multimode waveguide of width W_M, ridge (effective) refractive index n_r, and cladding (effective) refractive index n_c, the waveguide supports m lateral modes with mode numbers v = 0,1 ⋯ (m - 1) at free-space wavelength λ_0 which has the relation with $k_0 = \frac{2\pi}{\lambda_0}$. The lateral wave number k_{yv} and the propagation constant β_v are concerned with the ridge index n_r by the dispersion equation.

$$k_{yv}^2 + \beta_v^2 = k_0^2 n_r^2 \qquad \textbf{(2.2.1)}$$

$$k_{yv} = \frac{(v+1)\pi}{W_{ev}} \qquad \textbf{(2.2.2)}$$

The W_{ev} which means "effective" width takes into consideration the (polarization-dependent) lateral penetration depth of each mode field, related with the Goos-Hähnchen shifts at the ridge boundaries. To make high-contrast waveguides, the penetration depth is very small for $W_{ev} \simeq W_M$. In the **Eq. (2.2.3)**, the W_{ev} can be estimated by effective width W_{e0} (W_e for simplicity

corresponding to the fundamental mode).

$$W_{ev} \simeq W_e = W_M + \left(\frac{\lambda_0}{\pi}\right)\left(\frac{n_c}{n_r}\right)^{2\sigma}(n_r^2 - n_c^2)^{-(1/2)} \quad \textbf{(2.2.3)}$$

Where $\sigma = 0$ for TE and $\sigma = 1$ for TM. By the binominal expansion with $k_{yv}^2 \ll k_0^2 n_r^2$, the propagation constants β_v can deduced from

$$\beta_v \simeq k_0 n_r - \frac{(v+1)^2 \pi \lambda_0}{4 n_r W_e^2} \quad \textbf{(2.2.4)}$$

L_π as the beat length of the two lowest-order modes is represented as the propagation constant difference of two lowest-order modes in **Eq. (2.2.5)**.

$$L_\pi = \frac{\pi}{\beta_0 - \beta_1} \simeq \frac{4 n_r W_e^2}{3\lambda_0} \quad \textbf{(2.2.5)}$$

The propagation constants spacing between fundamental mode and mode (v) can be expressed as

$$(\beta_0 - \beta_v) \simeq \frac{v(v+2)\pi}{3L_\pi} \quad \textbf{(2.2.6)}$$

An input profile $\Psi(y, 0)$ imposed at $z = 0$ and entirely included within W_e will be separated into the modal field distribution $\Psi_v(y)$ in all modes.

$$\Psi(y, 0) = \sum_v c_v \Psi_v(y) \quad \textbf{(2.2.7)}$$

where the summation contains guided modes as well as radiative modes. The field excitation coefficient c_v can be estimated using overlap integrals based on the field–orthogonality relations.

$$c_v = \frac{\int \Psi(y,0)\,\Psi_v(y)dy}{\sqrt{\int \Psi_v^2(y)dy}} \quad \textbf{(2.2.8)}$$

If the "spatial spectrum" of the input field $\Psi(y,0)$ is narrow enough to prevent exciting unguided radiative modes, it can be decomposed concerning guided mode only,

$$\Psi(y,0) = \sum_{v=0}^{m-1} c_v \Psi_v(y) \quad \textbf{(2.2.9)}$$

The field profile at a distance z can be expressed as a superposition of all the guided mode field distributions.

$$\Psi(y,\mathrm{z}) = \sum_{v=0}^{m-1} c_v \Psi_v(y)\, exp[j(\omega t - \beta_v z)] \quad \textbf{(2.2.10)}$$

Assuming the time dependence $\exp(j\omega t)$ implicit, the field profile $\Psi(y,\mathrm{z})$ is represented as

$$\Psi(y,\mathrm{z}) = \sum_{v=0}^{m-1} c_v \Psi_v(y)\, exp[j(\beta_0 - \beta_v)z] \quad \textbf{(2.2.11)}$$

A useful expression for the field at a distance $z = L$ is found by substituting **Eq. (2.2.6)** into **Eq. (2.2.12)**. The form of $\Psi(y,L)$ will be determined by the modal excitation c_v and the properties of the mode phase factor.

$$\Psi(y,L) = \sum_{v=0}^{m-1} c_v \Psi_v(y)\, exp\left[j\frac{v(v+2)\pi}{3L_\pi}L\right] \quad \textbf{(2.2.12)}$$

Under certain circumstances, the field $\Psi(y,L)$ will be reproduce the input field $\Psi(y,0)$ due to the self-imaging mechanisms which are independent of the modal excitation. The properties

of this phenomenon are shown as

$$\nu(\nu+2) = \begin{cases} \text{even} & \text{for } \nu \text{ even} \\ \text{odd} & \text{for } \nu \text{ odd} \end{cases} \quad \textbf{(2.2.13)}$$

$$\Psi_v(-y) = \begin{cases} \Psi_v(y) & \text{for } v \text{ even} \\ -\Psi_v(y) & \text{for } v \text{ odd} \end{cases} \quad \textbf{(2.2.14)}$$

In **Eq. (2.2.12)**, $\Psi(y, L)$ will be an image of $\Psi(y, 0)$ if the condition of mode phase factor in **Eq. (2.2.15)** is satisfied.

$$\exp\left[j\frac{v(v+2)\pi}{3L_\pi}L\right] = 1 \text{ or } (-1)^v \quad \textbf{(2.2.15)}$$

The phase changes of all the modes along L must be different by integer multiples of 2π. In this case, all guided modes interfere with the same relative phases as in $z = 0$. That is, the image is a direct replica of the input field. Then, the phase changes must be alternatively even and odd multiples of π. In this case, the even modes will be in phase and the odd modes in antiphase. Due to the odd symmetry stated in **Eq. (2.2.13)** and **Eq. (2.2.14)**, the interference makes an image mirrored with respect to the plane $y = 0$.

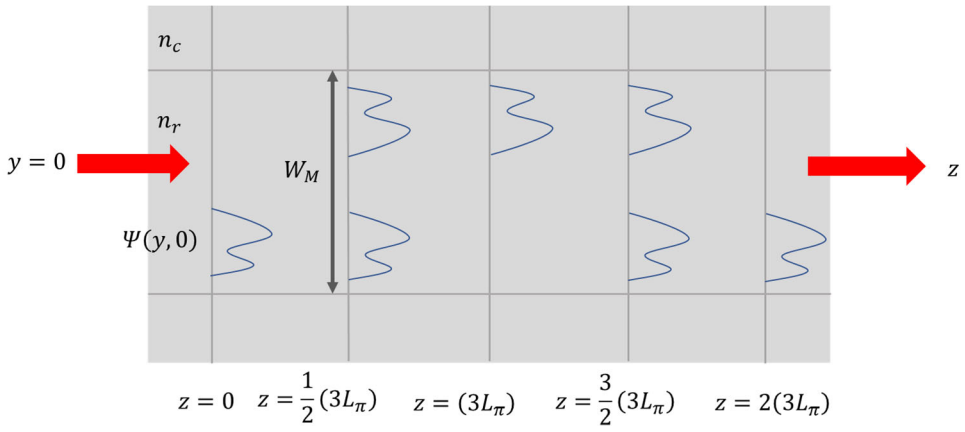

Fig. 2.4 Diagram of Multimode waveguide of the input field $\Psi(y, 0)$, mirrored single image at $(3L_\pi)$, a direct single image at $2(3L_\pi)$, and two-fold images at $\frac{1}{2}(3L_\pi)$ and $\frac{3}{2}(3L_\pi)$ [7].

By taking into account **Eq. (2.2.13)** and **Eq. (2.2.14)**, it is evident that the first and second condition of **Eq. (2.2.15)** will be fulfilled at $L = P(3L_\pi)$ with P = 0, 1, 2, ⋯ for P even and P odd, respectively. In addition to the single images at distances given by $L = P(3L_\pi)$, multiple images can be found as well. Let us consider the images obtained half-way between the direct and mirrored image positions, i.e., at distances $L = \frac{P}{2}(3L_\pi)$ with P = 1, 3, 5, ⋯ The total field at these lengths is found by substituting $L = \frac{P}{2}(3L_\pi)$ into **Eq. (2.2.12)**.

$$\Psi\left(y, \frac{P}{2}3L_\pi\right) = \sum_{v=0}^{m-1} c_v \Psi_v(y)\, exp\left[jv(v+2)p\left(\frac{\pi}{2}\right)\right] \qquad \textbf{(2.2.16)}$$

Considering the property of **Eq. (2.2.13)** and the mode field symmetry conditions of **Eqs. (2.2.14)** and **Eq. (2.2.16)** can be expressed as

$$\Psi\left(y, \frac{P}{2}3L_\pi\right) = \frac{1 + (-j)^p}{2}\ \Psi(y, 0) + \frac{1 - (-j)^p}{2}\ \Psi(-y, 0) \qquad \textbf{(2.2.17)}$$

Equation (2.2.17) indicates that a pair of images of Ψ $(y, 0)$, in quadrature and with amplitudes $\frac{1}{\sqrt{2}}$, at distances $z = \frac{1}{2}$, $(3L_\pi)$, $\frac{3}{2}(3L_\pi)$, ⋯ as shown in **Fig. 2.4**. This two-folded imaging can be applied to realize 2 x 2 3-dB couplers.

2.3 Evanescent coupling for design of UTC-PD

The proposed UTC-PD is designed using evanescent coupling structure. This structure is classified as a type of side-illuminated photodetector or edge-coupled photodetector.

Meanwhile, ahead of referring to the evanescent coupling structure, with repect to illuminated pattern at the photodetector, there are two types of photodetectors which are vertically-illuminate photodetector (VPD) and side-illuminate photodetector. The VPD is a conventional photodetector and it illuminates perpendicularly on the top of the optical device. However, the VPD has the limit of bandwidth-efficiency from a constraint at bandwidth-efficiency product. The bandwidth-efficiency tradeoff which ranges from 20 to 35 GHz in the VPD has been reported [9]. Therefore, due to these reasons, another type of the side-illuminated PD is used for UTC-PD design. The side-illuminated PD can be divided into several kinds of PDs which are waveguide PD, waveguide-fed PD, travelling-wave PD and periodic-travelling-wave PD, respectively [9].

Then, for making the UTC-PD, we considered the two optical coupling structures of butt-joint coupling and evanescent coupling in the type of waveguide-fed PDs. The basic concept of butt-joint coupling and evanescent coupling structure is shown as **Fig. 2.5**. As for the butt-joint coupling as shown in **Fig. 2.5 (a)**, the input light is confined at the core layer, and guided light along input waveguide is directly coupled and absorbed into photoabsorption layer. The additional layers for the light coupling between the input waveguide and the photodiode are not required and the width of the photodiode can be remarkably reduced by a fully absorbed light with a high quantum efficiency [10]. However, the butt-joint coupling structure needs several regrowth processes in the fabrication [11].

In the evanescent coupling structure as shown in **Fig. 2.5 (b)**, the guided light along the core layer in the input waveguide is evanescently coupled with moving up to photoabsorption layer which is located on waveguide layer. Though, at the evanescent coupling, a practical optical coupling efficiency requires a longer PD which causes a large capacitance and fail to get a high frequency response, a better distribution of photogenerated carriers can be achieved

due to a progressive absorption [12]. Furthermore, a higher power is expected through the photodiode mesa which is shown on the top of the waveguide with photoabsorption layer. Thus, the mesa structure of the photodiode can attain more uniform absorption from guided single mode at the input waveguide [13].

At a prospective use of the PD, enough optical input power could be provided from light sources and thus, a higher photoabsorption uniformity is preferable rather than a higher coupling efficiency. Then, we chose the evanescent coupling structure since the butt coupling structure has difficulties on epitaxial regrowth in device fabrication process.

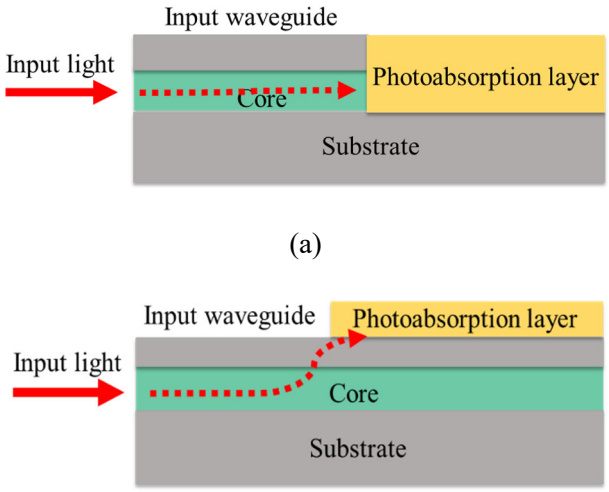

Fig. 2.5 Schematics of two coupling structure. (a) Butt-joint coupling. (b) Evanescent coupling.

2.4 Phased array antenna

The arrayed photomixers in the proposed generator module are designed based on the principle of phased array antenna because we aimed to combine the generated terahertz wave at each antenna in phase. The phased array antenna is generally used at the field of the radar or communication system [14-15]. First of all, **Figure 2.6** shows equally spaced linear array

antennas which are aligned with the spacing *d* and the same phase.

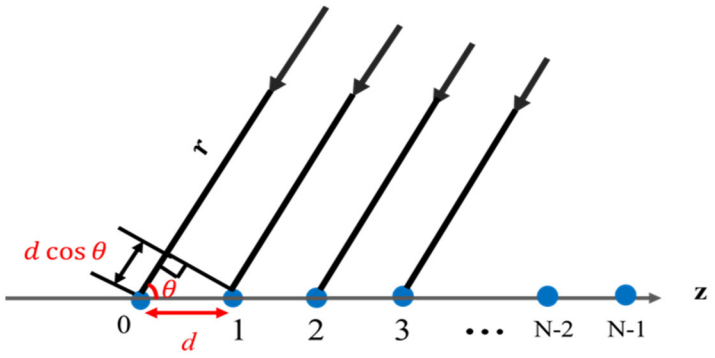

Fig. 2.6 Schematic of equally spaced linear array of isotropic point sources [14].

The array factor (AF) at the phased array antenna is expressed as **Eq. (2.4.1)**. **Equation (2.4.3)** is obtained when we set ψ as progressive phase shift, α as phase difference between adjacent elements as represented in **Eq. (2.4.2)**. The electronic scanning phased array is operated by the mechanism, which indicates that the maximum radiation at the arrayed antennas can be originated in any desired direction to formulate a scanning array by controlling the progressive phase with cancellation of the radiated beams in undesired direction [16-17]. Then, the beams are steered in the desired direction.

$$\mathrm{AF} = \sum_{n=0}^{N-1} E_n \quad e^{jn(\beta d\cos\theta+\alpha)} \tag{2.4.1}$$

$$\psi = \beta\, d\cos\theta + \alpha \tag{2.4.2}$$

$$\mathrm{AF} = \sum_{n=0}^{N-1} E_n \quad e^{jn\psi} \tag{2.4.3}$$

The amplitude of each current at each element is assumed for the linear antenna array. The **Eq. (2.4.3)** is paraphrased as shown in **Eq. (2.4.4)** and **Eq. (2.4.5)**

$$\mathrm{AF} = E_0 \sum_{n=0}^{N-1} E_n \;\; e^{jn\psi} = E_0(1 + e^{j\psi} \cdots + e^{j(N-1)\psi} \;\;) \tag{2.4.4}$$

$$\mathrm{AF} \;\; e^{j\psi} = E_0(e^{j\psi} + e^{j2\psi} \cdots + e^{jN\psi}) \tag{2.4.5}$$

From subtraction between the two equations above, **Equations (2.4.6a)-(2.4.6d)** are obtained.

$$\mathrm{AF} \;\; = \frac{1 - e^{jN\psi}}{1 - e^{j\psi}} E_0 \tag{2.4.6a}$$

$$= E_0 \frac{e^{jN\psi} - 1}{e^{j\psi} - 1} \tag{2.4.6b}$$

$$= E_0 \frac{e^{jN\psi/2}}{e^{j\psi/2}} \frac{e^{jN\psi/2} - e^{jN\psi/2}}{e^{j\psi/2} - e^{jN\psi/2}} \tag{2.4.6c}$$

$$= E_0 e^{j(N-1)\psi/2} \frac{\sin(\frac{N\psi}{2})}{\sin(\frac{\psi}{2})} \tag{2.4.6d}$$

Without considering $e^{j(N-1)\psi/2}$, the array factor becomes maximized at $\psi = 0$ and the relation is expressed as **Eq. (2.4.7)**

$$\mathrm{AF} = E_0(1 + 1 \cdots + 1 \;\;) = E_0 N \tag{2.4.7}$$

Finally, the uniform excited, equally spaced linear arrays (UE, ELSA) are described as shown in **Eq. (2.4.8)**. The directivity of uniformly excited is determined by **Eq. (2.4.9).** The directivity of the antenna describes the magnitude of the peak level at the radiated wave. Each variable means interelement α, phase constant β, number of elements N and excess phase array δ,

respectively. The directivity depending on d/λ at N elements is calculated using the equation as shown in **Fig. 2.7.**

$$f(\psi) = \frac{\sin(\frac{N\psi}{2})}{N\sin(\frac{\psi}{2})} \tag{2.4.8}$$

$$D = \frac{\left|\frac{\sin(N\delta/2)}{N\sin(\delta/2)}\right|^2}{\frac{1}{N} + \frac{2}{N^2}\sum_{m=1}^{N-1}\frac{N-m}{m\beta d}\sin m\beta d\cos m\alpha} \tag{2.4.9}$$

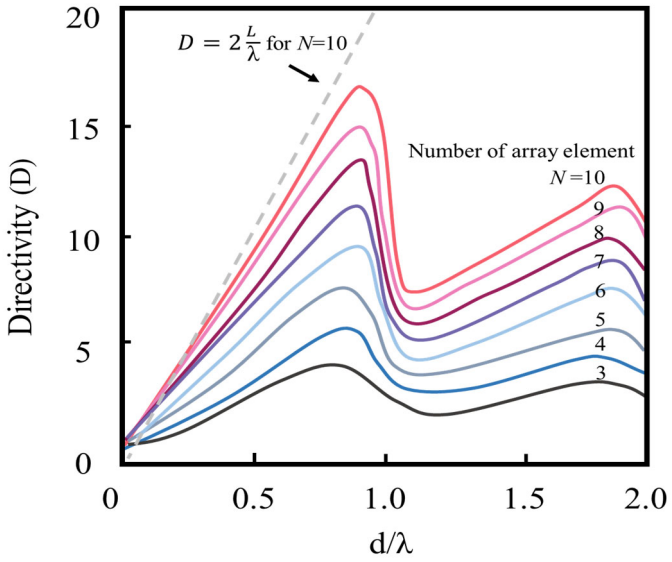

Fig. 2.7 Directivity at equally spaced linear array of isotropic point sources [14].

With the relation above, we determine the spacing between each antenna. The spacing d of our integrated device is optimized when d/λ is equal to 0.5. Therefore, for the device of 600 GHz operation, the 250 μm-wide spacing antennas should be designed. Based on the explained phased array antenna, the expected combined THz-power at the phased array antennas can be calculated according to **Eqs. (2.4.10a)-(2.4.10b)**. The α is obtained at $\psi = 0$ of the

maximum of array factor.

$$\mathrm{P} = \left| \sum_{n=0}^{N-1} E_n \quad e^{jn(\beta d cos\theta + \alpha)} \right|^2 \qquad \textbf{(2.4.10a)}$$

$$\alpha = -\beta d cos\theta \qquad \textbf{(2.4.10b)}$$

The combined peak power which indicates the product between the square of the array element and the square of the electric field amplitude is expressed as **Eq. (2.4.11)**

$$\mathrm{P} = |\mathrm{N}|^2 |\mathrm{E}|^2 \qquad \textbf{(2.4.11)}$$

In this thesis, we demonstrate the relation referred in **Eq. (2.4.11)** at the proposed THz-wave generator using the arrayed antennas. The phased array antenna also has advantages of higher directivity from larger number of element array. It is available to radiate multiple beams simultaneously for transmitting multifunctional operations even though it has disadvantage such as high cost and complexity for a large scale of realization, etc [18]. Because of the necessity of phase matching between array elements, there have been challenges for overcoming the drawbacks of the system with the control at phase shifters [19-21]. Furthermore, the two- and three-dimensionally realized array antennas have been developed for application to wireless communication system [22]. In this research, the integrated devices are designed with considering above issues.

2.5 Conclusions

In this chapter, basic theories and concepts for the design of each component at the integrated devices were explained. Firstly, the optical waveguide theory was introduced due to the optical devices are based on the optical waveguide structure. The optical waveguide should be composed of carefully chosen refractive index, modes, polarizations and other parameters. Secondly, in the MMI design, the information of both length and width of the MMI, modes and other conditions can be a dominant factor. Thirdly, the concept of evanescent coupling and butt-joint coupling was described. We chose the evanescent coupling structure for the merit of the fabrication process and a uniform absorption in the absorption layer. Finally, the theory of phased array antenna was explained. The proposed arrayed photomixers have each antenna. The spacing of the photomixers integrated with antennas is designed by the phased array antenna.

References

[1] D. Murcues, “Theory of dielectric optical waveguides,” Academic Press, New York, Chap. 1,1974.

[2] K. Okamoto, “Fundamental of optical waveguides,” Second edition, Academic Press, New York, Chap. 2, 2006.

[3] C. R. Doerr and H. Kogelnik “Dielectric waveguide theory,” IEEE/OSA, J. Light. Technol, vol. 26, no. 9, pp. 1176-1187, May. 2008.

[4] J. C. Maxwell, “On physical lines of force,” The London, Edinburgh, and Dublin Philos. Mag. J. Sci., p.161, 1861.

[5] R. E. Nahory, M.A. Pollock, W.D. Johnston, Jr., and R.L. Barns, “Band gap versus composition and demonstration of Vegard’s law for $In_{1-x}Ga_xAs_yP_{1-y}$ lattice matched to InP,” Appl. Phys. Lett, 33, 659, 1978.

[6] B. Broberg and S. Lindgren, “Refractive index of $In_{1-x}Ga_xAs_yP_{1-y}$ layers and InP in the transparent wavelength region,” J.Appl. Phys, vol.55, no.9, May. 1994.

[7] L. B. Soldano and E. C. M. Pennigs, “Optical multi-mode interference devices based on self-imaging: principles and applications,” J. Light. Technol, vol. 13, no. 4, pp. 615-627, Apr. 1995.

[8] M. Bachmann, P. A. Besse and H. Melchior, “General self-imaging properties in N x N multimode interference couplers including phase relations.” Appl. Opt, vol. 33, no. 18, pp. 3905-3911, Jun. 1994.

[9] K. Kato, “Ultrawide-band/high-frequency photodetectors,” IEEE Trans. Microwave Theory Tech., vol. 47, no. 7, pp. 1265-1281, Jul. 1999.

[10] A. Umbach, M. Leone, and G. Unterbörsch, “High-frequency behavior of waveguide integrated photodiodes monolithically integrated on InP using optical butt coupling,” J. Appl. Phys, vol.81, no.6, Mar. 1997.

[11] J. B. D. Soole, Y. Silberberg, A. Scherer, H. P. LeBlanc, N. C. Andreadakis, and C. Caneau, “Fast high-efficiency integrated waveguide photodetectors using novel hybrid vertical/butt coupling

geometry," Appl. Phys. Lett, vol. 61, pp. 13-15, 1992.

[12] M. Achouche, V. Magnin, J. Harari, F. Lelarge, E. Derouin, C. Jany, D. Carpentier, F. Blache, and D. Decoster, "High performance evanescent edge coupled waveguide uni traveling-carrier photodiodes for > 40-Gb/s optical receivers," IEEE photon. Technol. Lett, vol. 16, no. 2, Feb. 2004.

[13] A. Beling and J. C. Campbell, "InP-based high-speed photodetectors," J. Light. Technol, vol. 27, no. 3, pp. 343-355, Feb. 2009.

[14] W. L. Stuzman and G.A. Thiele, " Antenna theory and design," John Wiley & Sons, Third edition, 2013.

[15] R. C. Hansen, "Phased Array Antennas," Wiley Press, Second edition, Nov. 2009.

[16] C. A. Balanis, "Antenna Theory: Analysis and Design." John Wiley & Sons, 4th edition, 2015.

[17] D. Parker and D. C. Zimmermann, "Phased arrays- Part1: Theory and architectures," IEEE Trans, Micro Theory Tech, 50, pp.678-687, 2002.

[18] L. C. Godara, "Applications of Antenna Arrays to Mobile Communications, Part I: Performance Improvement, Feasibility, and System Considerations," Proceedings of the IEEE, vol. 85, no. 8, pp. 1193–1245, 1997.

[19] S. Ohmori, "Phased array antennas for mobile communications," Annales Des Télécommunications, vol. 54, pp.93–102, 1999.

[20] D. Ehyaie and A. Mortazawi, "A New Approach to Design Low Cost, Low Complexity Phased Arrays," IEEE MTT-S International Microwave Symposium, pp.1270-1273, 2010.

[21] A. Tombak and A. Mortazawi, "A novel low-cost beam-steering technique based on the extended-resonance power-dividing method," IEEE. Transactions on Microwave Theory and Techniques, vol. 52, no.2, pp. 664-670, Feb. 2004.

[22] A.Vesa, F. Alexa, and H. Baltă, "Comparisons between 2D and 3D Uniform Array Antennas," Proceedings of the Federated Conference on Computer Science and Information Systems, pp. 1285–1290, 2015.

3. Arrayed photomixers

3.1 Waveguide for photomixer design

Each photomixer of the proposed arrayed photomixers was designed using an optical waveguide as referred in Chapter 2. The optical waveguide is a fundamental element to make an optical device and it largely influences on an efficiency of the integrated device. The optical waveguide composed of Ⅲ-Ⅴ semiconductor is suitable for making the photonic integrated devices which include the UTC-PD [1]. We used InP/ InGaAsP material system based on Ⅲ-Ⅴ semiconductor. Because the integrated UTC-PD is designed for the detection of the lightwave with 1.55 μm wavelength. The waveguide for our design basically has a vertical structure that includes a substrate of InP layer, InGaAsP core layer and InP cladding layer in the InP/InGaAsP material system as shown in **Fig. 3.1**. To determine the thickness of core layer and cladding layer in terms of an efficiency or a loss of the device is important. Investigating the optical field distribution of the waveguide is needed for a light confinement at the core layer. On the other hand, unnecessary optical field leakage to the under mesa which is defined as the waveguide region by etching causes the optical loss of the guided light at a bending waveguide. Less confinement factor in the under mesa can be preferable for a low leakage of the light guided by the core layer. With this assumption, to figure out the confinement factor at the under mesa can be an indirect method to estimate waveguide features. It is significant to find the best combination of the thickness of both core layer and cladding layer. Each confinement factor was calculated by one-dimensional simulation that enables the convenient calculation even though the concept of confinement factor at the under mesa perfectly coincides with an efficiency or a loss at the device.

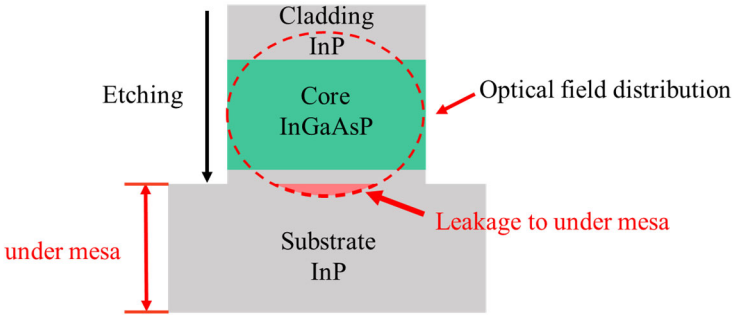

Fig. 3.1 Optical leakage to under mesa at waveguide structure**.**

The confinement factor was simulated at 1.55 μm wavelength and polarization of TE mode. Several kinds of core layer thicknesses we set were used in the calculation and those thicknesses are 0.17 μm, 0.28 μm, 0.39 μm, 0.5 μm, and 0.61 μm with considering entire thickness of cross-sectional structure.

Firstly, two types of refractive indices at core layer were investigated. The refractive index of all InP layers was set at 3.17 and that of InGaAsP quaternary layer was calculated by the method as explained in Chapter 2.1 [2]. The calculated refractive indices are $n_c \simeq 3.435$ for bandgap wavelength of 1.40 μm and $n_c \simeq 3.404$ for bandgap wavelength of 1.38 μm. With setting each refractive index and each core layer thickness, the confinement factor by the change of etching depth and cladding layer thickness was simulated. An available range of the thickness of cladding layer and etching was determined by the limitation of vertical width to be fixed. **Figure 3.2** shows the confinement factor depending on the etching depth and the thickness of cladding layer at each core layer thickness. From the simulated results, we can assume that the relation between the core layer thickness and the confinement factor is inverse proportion. Then, at each core layer thickness shown in **Fig. 3.2 (a-b), (c-d), (e-f), (g-h)** and **(i-j),** the two results between the two refractive indices of $n_c \simeq 3.435$ and $n_c \simeq 3.404$ at the core layer also represent that the structure which has slightly higher refractive index of the core

layer tends to get a lower confinement factor at the undermesa. In terms of the refractive index, this can be explained from numerical aperture based on the contrast by difference of refractive index at the core layer and cladding layer [3]. The higher contrast between the two layers results in the higher confinement at the core layer with the reduction of optical leakage to the undermesa.

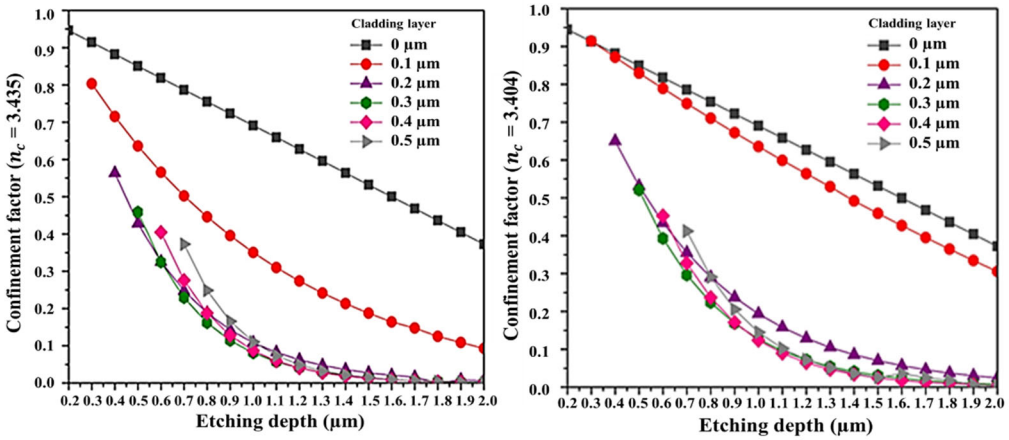

(a)

(b)

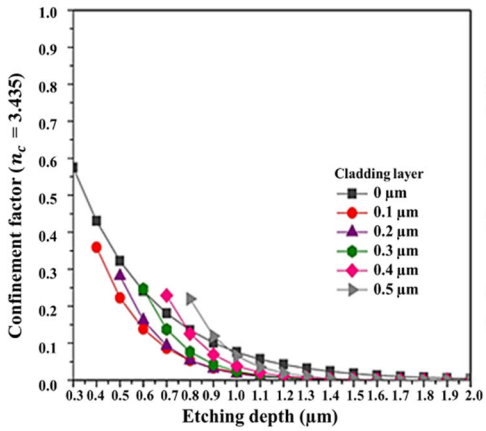

(c)

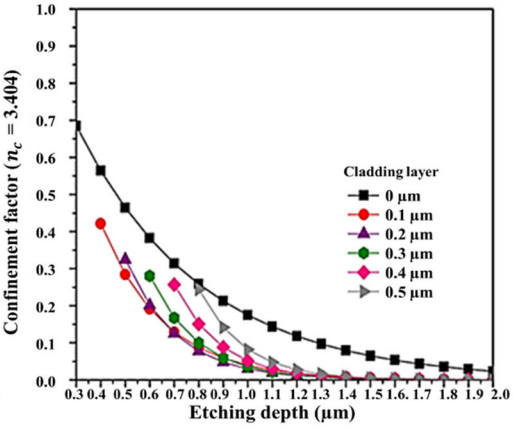

(d)

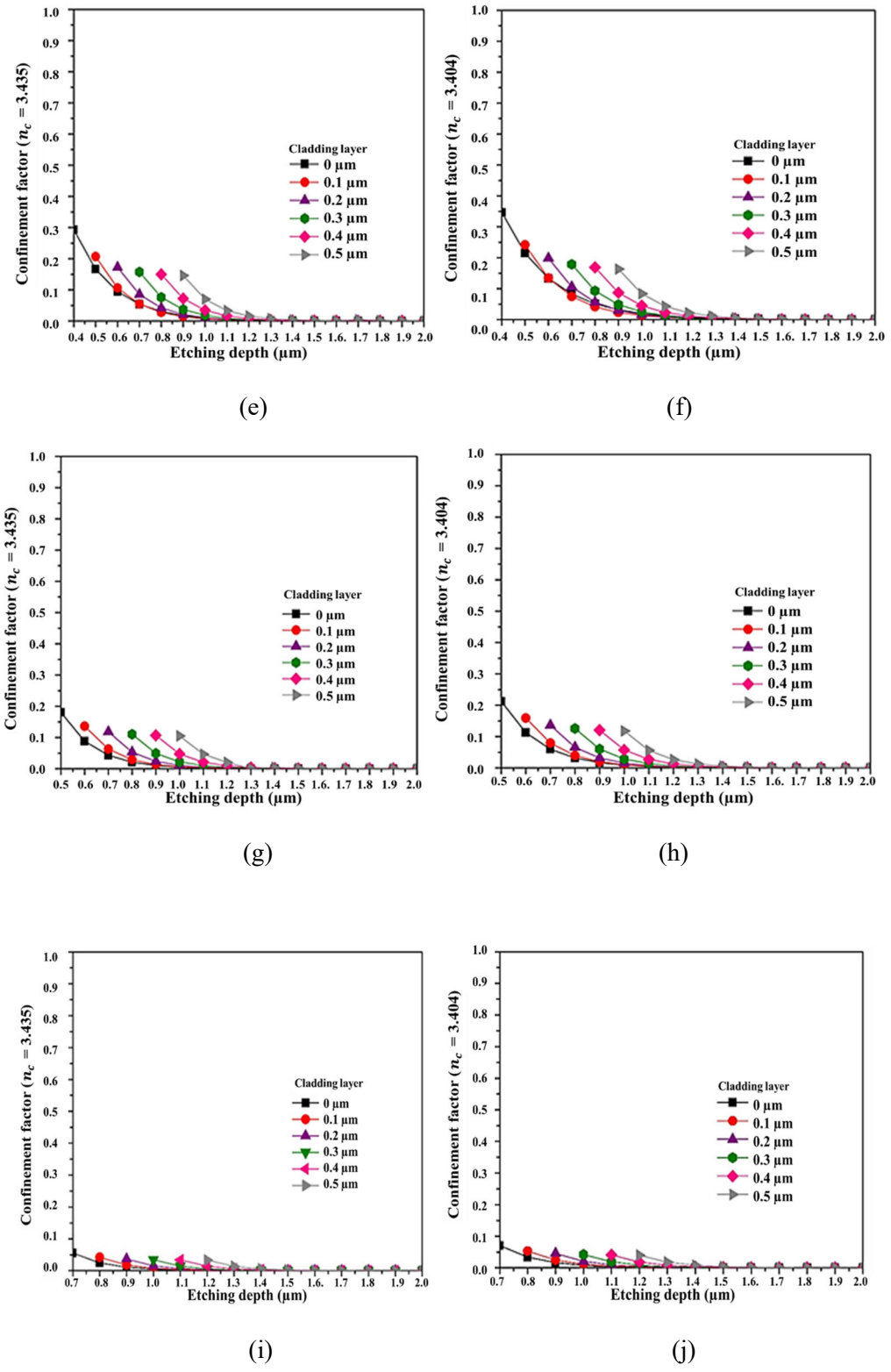

Fig. 3.2 Each confinement factor at undermesa with core layer thickness. (a-b) 0.17-μm-thick core. (c-d) 0.28-μm-thick core. (e-f) 0.39-μm-thick core. (g-h) 0.5-μm-thick core. (i-j) 0.61-μm-thick core.

Firstly, the result in **Fig. 3.2 (a)** and **Fig. 3.2 (b)** shows the maximum confinement factor of 0.95 at the structure without cladding layer and also a high confinement factor at 0.1 μm-thick cladding layer in common. Too thin cladding layer and core layer caused the high confinement factor to the undermesa. In case of 0.17 μm- thick core layer, almost confinement factors at each cladding layer thickness were high compared to those of other thicknesses. Therefore, the necessity to increase the thickness of core layer is needed for a low confinement at the undermesa. Secondly, in the result of 0.28 μm- thick core layer as shown in **Fig. 3.2 (c)** and **Fig. 3.2 (d)**, the confinement factor was lessened at the same cladding layers due to increased core layer thickness. The maximum without cladding layer was around 0.57 in **Fig. 3.2 (c)** and 0.69 in **Fig. 3.2 (d)**, respectively. The confinement factors at each cladding layer were decreased compared to those of 0.17 μm- thick core layer.

Then, **Fig. 3.2 (e)** and **Fig. 3.2 (f)** shows the confinement factor at 0.39 μm- thick core layer. The confinement factor at both refractive indices is about 0.29 in **Fig. 3.2 (e)** and 0.34 in **Fig. 3.2 (f)** at the maximum and the results also showed similar distribution patterns. The confinement factor at 0.5 μm-thick core layer represented 0.18 in **Fig. 3.2 (g)** and 0.21 in **Fig. 3.2 (h)** at the maximum with the same distribution. Finally, the confinement factor at 0.61 μm-thick core layer showed the maximum of 0.05 in **Fig. 3.2 (i)** and 0.07 in **Fig. 3.2 (j)**. The thicker thickness of the core layer provides the lower confinement factor in the results. The refractive index of core layer does not seriously affect to the confinement factor in comparison with other dominant factors such as etching depth, the thickness of core layer and cladding layer. Based on the results, we concluded that the features of the waveguide structure can be determined by dominant three factors referred above.

As for the result of etching depth as shown in **Fig. 3.2**, the confinement factor at the undermesa decreases with etching depth. Thus, a deep etching depth enables the optical field at the core layer makes more clearly by reducing an optical leakage to the undermesa. However, considering the etching depth, it has not to be deep due to the limitation for device fabrication process. Therefore, the optimal combination of the core layer and the cladding layer was also investigated. At first, the thickness of 0.28 μm, 0.39 μm and 0.5 μm at the range of the core layer was considered to be chosen as part of expected combination. Because the confinement factor of 0.17 μm-thick core layer in **Fig. 3.2 (a)** and **Fig. 3.2 (b)** showed more than 0.9 that describes an excessive leakage while that of 0.61 μm-thick core layers in **Fig. 3.2 (i)** and **Fig. 3.2 (j)** has a possibility to introduce higher order modes that fail to a single mode operation due to too wide thickness even though it represented the minimum confinement factor. Then, based on the core layer thicknesses we chose, a suitable combination of core layer and cladding layer thickness is described as 0.28 μm-thick core layer with 0.1μm-thick cladding layer, 0.39 μm-thick core layer with no cladding layer or 0.1 μm-thick cladding layer, and 0.5 μm-thick core layer with no cladding layer.

Consequently, two acceptable combinations for waveguide structure in our design, 0.28-μm-thick core layer ($n_c = 3.435$) with 0.1-μm-thick cladding layer and 0.5-μm-thick core layer ($n_c = 3.404$) without cladding layer. The refractive index of the core layer at each combination was chosen according to a lower confinement in the simulated results. We concluded that the condition of the 0.28 μm-thick core layer with more than 1.2 μm etching and 0.5 μm-thick core layer with etching over 1 μm leads to confinement factor to be zero at the undermesa. The chosen waveguide structures and their etching depth are shown in **Fig. 3.3**. We call each structure as 3-layered structure and 2-layered structure, respectively, for convenience. For the next step, the referred etching depth ranges can be also regarded as an

available etching depth for designing bending waveguide which is used at optical paths in the photomixer chip. However, they can be determined differently in reality at the fabrication process unlike our expectation since each optical component has their own etching depth. Using the two types of waveguide structures, we investigated the properties and the optimized structure of the optical component for designing entire device.

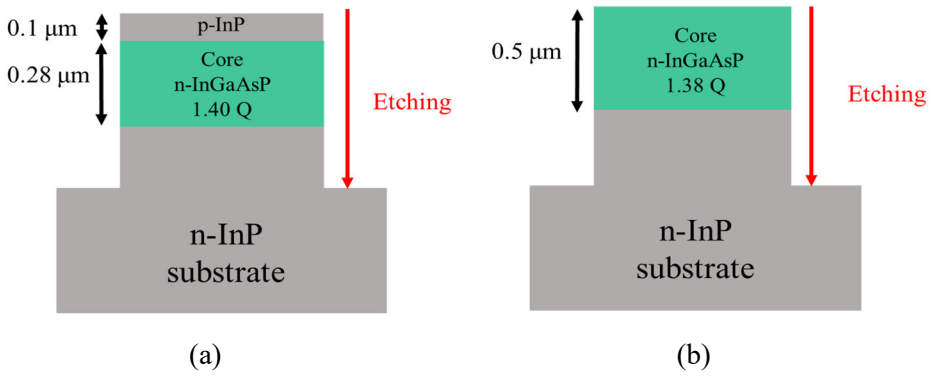

Fig. 3.3 Chosen waveguide structures for photomixer design. (a) 3-layered structure. (b) 2-layered structure.

3.2 Design of bending waveguide

Bending waveguide is designed to be connected to optical splitter outputs and it can be more direct evaluation than confinement factor in estimation of coupling loss at waveguide structure. A low loss bending waveguide is required because the bending structure may cause optical coupling loss at the integrated device. Therefore, the number of bending sections should be minimized as possible. For the bending waveguide design, we used the waveguide structures chosen in the Chapter 3.1. **Figure 3.4** shows a schematic of bending waveguide which has curvatures of radius r with 90 degree at two 1 μm-wide bending sections and two straight sections with 1 μm width. At the joint between the two sections, radiation loss, transition loss

and phase constant of the propagating bending waveguide are importantly considered [4]. Transition loss is regarded as the most important factor among the three factors. The transition loss and higher order mode excitation can be caused by the field mismatch at the waveguide [5]. Due to the matched bend, the transition loss and a distortion out of field can be reduced [6]. Thus, for a low loss bending waveguide, we need to find the transition loss or the bending efficiency at two suggested waveguide structures. Also, the simulated result between the structures should be compared with each other.

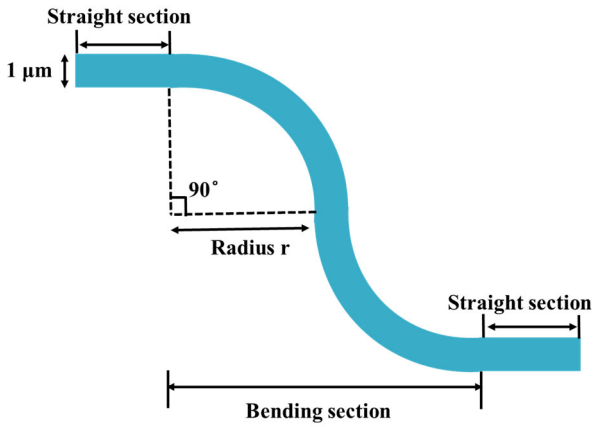

Fig. 3.4 Schematic of bending waveguide.

There are some factors which have an effect on the bending efficiency such as bending radius, etching depth, offset between each joint, etc. Firstly, we investigated the dependency on the radius with 30 μm, 40 μm and 50 μm and that on etching depth in the bending efficiency. **Figure 3.5** shows the simulated results of the bending efficiency. The result as shown in **Fig. 3.5 (a)** represented the bending efficiency on 3-layered structure. The bending efficiency increases with etching depth. But it is saturated above 1.6 μm etching depth. The optimized radius of 30 μm-wide with the etching depth from 1.0 μm to 1.6 μm was chosen while the efficiency at each radius shows much difference. The maximum bending efficiency of 0.95 was

obtained at 1.9 μm etching depth with the optimized radius of 30 μm. **Figure 3.5 (b)** shows that the bending efficiency increases from 0.5 μm to 1 μm etching depth at the 2-layered structure. The efficiency on each radius becomes saturated at more than 1 μm etching depth. We obtained the maximum efficiency of 0.92 at 50 μm-wide bending radius and 1 μm etching depth. We confirmed that the etching depth and the radius concerning bending efficiency can be dominant factors at the two waveguide structures.

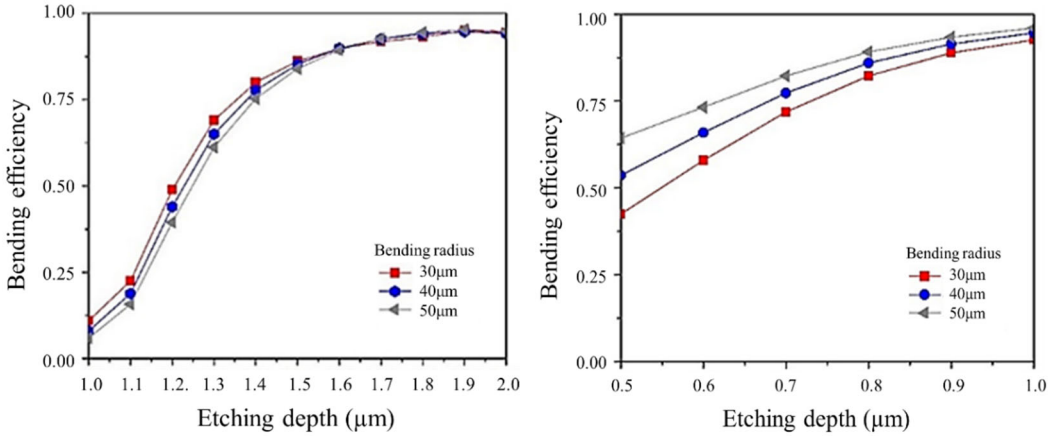

(a) (b)

Fig. 3.5 Relation between etching depth and bending efficiency with bending radius. (a) 3-layered structure. (b) 2- layered structure.

Then, we introduced a lateral offset at each joint for reduced transition loss between the straight and bending section [7-8]. The offset is defined at the boundaries of each joint and it is dislocated as shown in **Fig. 3.6**. **Figure 3.7** shows that both waveguide structures were optimized with the maximum efficiency at 0.02 μm-wide offset and 2 μm etching depth. The maximum efficiency was obtained as 0.95 of the 3-layered structure and 0.98 of the 2-layered structure. The efficiency reduction after 0.02 μm-wide offset indicates that the 0.02 μm-wide offset is applicable to any other types of waveguide structures. Finally, we achieved the bending

efficiency enhancement by introducing an appropriate offset in bending waveguide as one of the solutions to reduce the transition loss or to obtain a higher bending efficiency.

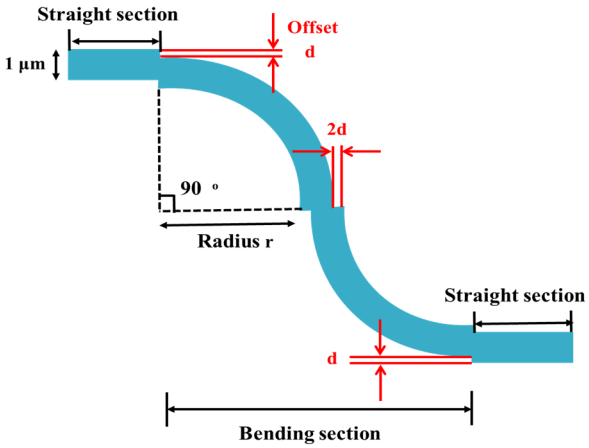

Fig. 3.6 Schematic of offset defined as d at the boundary between straight section and bending section, and 2d at the boundary between bending sections.

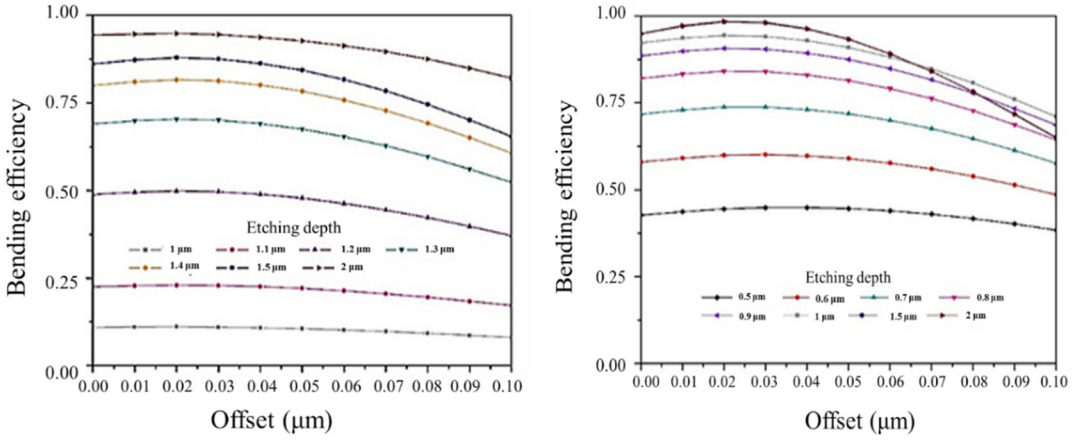

(a) (b)

Fig. 3.7 The relation between bending efficiency and offset. (a) 3-layered structure. (b) 2-layered structure.

From the simulated results, we found that several parameters such as etching depth, radius and offset have an influence on the bending efficiency. Among the parameters, the etching depth was a great influence on the bending efficiency compared to other parameters. This is explained

by the fact that deep etching brings a higher efficiency and the propagated guided light along core layer without unnecessary loss caused by dispersion to the under mesa can be possible. On the other hand, a reasonable etching depth is essential for making a real device.

Then, for a conclusive information to make the bending waveguide, the bending efficiency at the two waveguide structures was simulated. We investigated the dependency on thickness of cladding layer at the 3-layered structure and that of core layer at the 2-layered structure, respectively. In this simulation, the 1.9 μm etching depth which is the best etching depth for the 3-layered structure was equally used in the two calculations for comparison under the same condition. First of all, the bending efficiency of the 3-layered structure was calculated with changing cladding layer thickness as shown in **Fig. 3.8 (a)**. The change of only cladding layer was simulated for simplicity although the core layer can be also a parameter. The efficiency of fixed 0.1 μm-thick cladding layer thickness is lower than that of 0.2 μm-thick cladding layer thickness, which has a maximum bending efficiency of 0.97. Thus, 0.2 μm-thick cladding layer thickness has merits for a better coupling or a low bending loss in the bending waveguide.

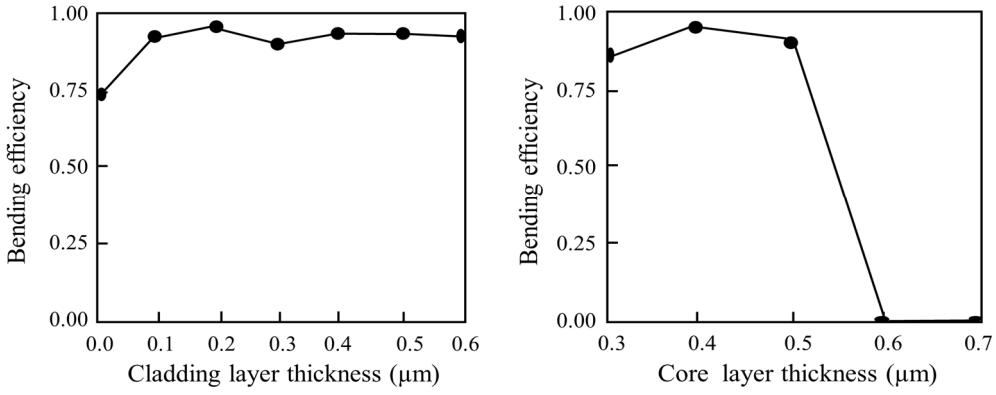

(a) (b)

Fig. 3.8 Bending efficiency. (a) 3-layered structure. (b) 2-layered structure.

Meanwhile, **Figure 3.8 (b)** shows the bending efficiency of the 2-layered structure depending on core layer. This time we assumed that the thickness of cladding layer in the waveguide structure should be existed on the 0.5 μm-thick core layer even though the 0.5 μm-thick core layer showed the best combination with no cladding layer as discussed in Chapter 3.1. The bending efficiency with change of core layer thickness was calculated. Only core layer was investigated for simplicity even though the thickness of the cladding layer can be a parameter. The simulated result as shown in **Fig. 3.8 (b)** represented that the bending efficiency of 0.97 at 0.4 μm-thick core layer is higher than that of 0.95 at 0.5 μm-thick core layer. Based on the simulated each bending efficiency, the total efficiency of the photomixer device will be estimated with photoabsorption efficiency at evanescently coupled UTC-PD in Chapter 3.4.

3.3 Multimode interference splitter

We designed the MMI splitter as power divider in the optical path for distributing the same power from optical input power. The MMI splitter by self-imaging phenomenon as power divider can have the input field branching on a very small area [9]. Each 1x2 MMI splitter was designed so that the optical power is simultaneously distributed into a pair of UTC-PDs. The 1x2 MMI splitter consists of one input, multimode waveguide in the center and two outputs as shown in **Fig. 3.9**. The MMI splitter has 1.2 μm-wide input and two outputs.

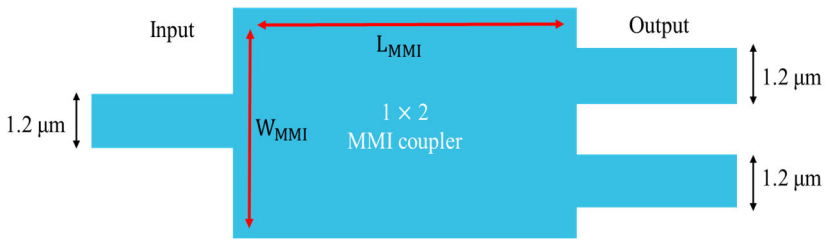

Fig. 3.9 Plan view of 1x2 MMI splitter.

As for the simulation of the MMI, we aimed to attain an equal power distribution into each output and the same maximum power. Also, based on the MMI theory mentioned in Chapter 2.2, the output power or the optical splitting efficiency at the MMI should be considered irrespective of vertical structures of waveguides. That is, the MMI is almost independent of vertical waveguide structure while the length and the width of the MMI are dominant factors to make the optimized splitter. Firstly, the output power and the characteristics of the ideal MMI were investigated to find the optimized length and width. The ideal MMI with an infinite etching at the two waveguide structures is shown in **Fig. 3.10 (a)** and **Fig. 3.10 (b)**, and the entire MMI structure is suggested in **Fig. 3.10 (c)**.

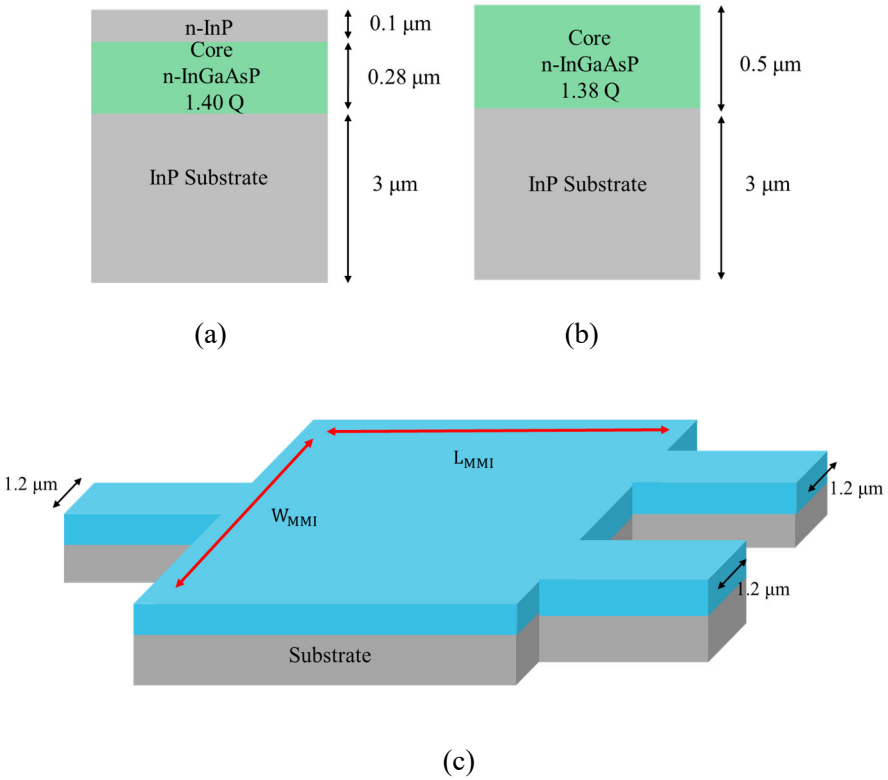

Fig. 3.10 Schematic of ideal MMI. (a) 3-layered structure. (b) 2-layered structure. (c) Entire view of ideal MMI with an infinite etching depth.

The simulated results proved that the two structures have the same range of the width from 6.3 μm to 6.5 μm and the length from 42 μm to 44 μm for the MMI design. Because a high power at the sum of two outputs with a uniform power was obtained as shown in **Fig. 3.11**.

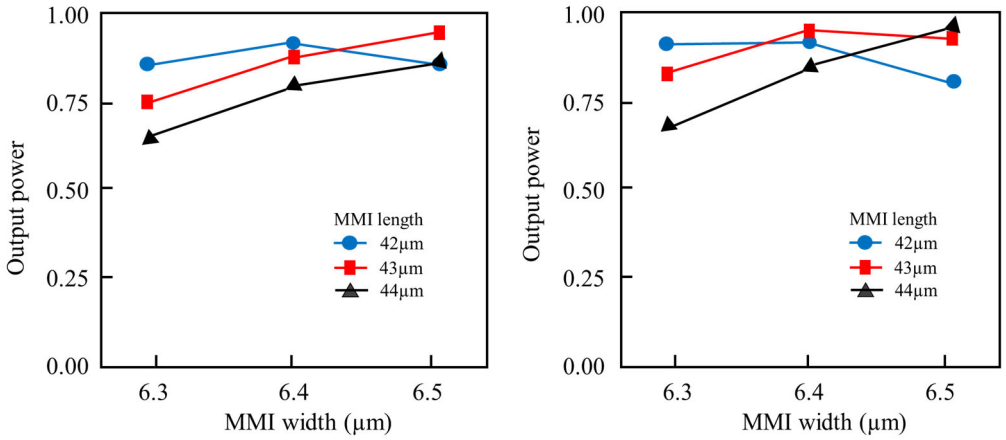

Fig. 3.11 Output power as a function of MMI width at an ideal MMI splitter. (a) 3-layered structure. (b) 2-layered structure.

The MMI for the 3-layered structure was optimized at 43 μm-long and 6.5 μm- wide MMI with maximum efficiency of about 0.96 as shown in **Fig. 3.11 (a)**. Similarly, the maximum efficiency of nearly 0.96 at the 2-layered structure was obtained by the length of 43 μm and the width of 6.4 μm in **Fig. 3.11 (b)**. With these results, we confirmed that the length of 43 μm can be applied to both MMI though the optimized width was slightly different. This result does not completely correspond to the previous assumption that the MMIs have the optimized length and width without considering their vertical structures. Thus, other parameters to influence on the optimized structure of the MMIs should be investigated. In this research, we focused on the etching depth among various parameters since we already have confirmed the importance in the Chapter 3.1 and 3.2. Furthermore, it is needed to be fixed for device fabrication process.

Figure 3. 12 (a) shows the output power of the two waveguide structures depending on the etching depth. In the 3-layered structure, the output power has a fluctuation in the range less than 2.2 μm etching with a low power. However, the 2-layered structure is not sensitive on the etching depth. Due to the results, the MMI at the 3-layered structure should be more deeply etched than the bending waveguide with the maximum efficiency at 1.9 μm etching discussed in Chapter 3.2. The etching depth of the MMI using 3-layered structure can be considered larger than that of bending waveguide for device fabrication. But too deep etching which is more than 2.2 μm is not efficient on the device fabrication process. Therefore, we conclude that 2.2 μm etching depth can be suitable for the 3-layered structure. Also, the 1 μm-deep etching with maximum bending efficiency and the 1 μm etching of the MMI in the 2-layered structure can be used to make the integrated device. Finally, we compared the output power at the two structures using 2.2 μm etching depth because the depth showed approximately the maximum power at both structures. Using the depth, the optimized width of each MMI at both structures with fixed MMI length of 43μm was simulated.

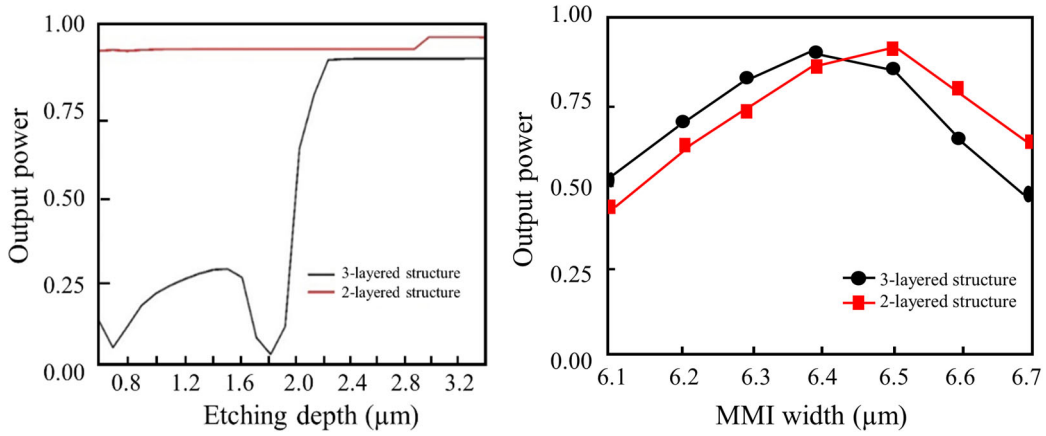

Fig. 3. 12 Output power as a function of (a) Etching depth and (b) MMI width.

Figure 3.12 (b) shows the maximum power of nearly 0.92 at 6.5 μm-wide MMI in the 3-layered structure and that of about 0.93 at 6.4 μm-wide MMI in the 2-layered structure. The optimized width of both MMIs corresponded to that of the ideal 1x2 MMI splitters. In conclusion, in this chapter, we found that the optimized width and length at the 1x2 MMIs has a similarity without the influence on the factor of cross-sectional structure of the MMI.

3.4 Evanescently coupled photodiode

Finally, in Chapter 3.4, the photomixer design to make the UTC-PD is explained. For the UTC-PD design, we used the evanescent coupling mechanism described in Chapter 2.3. The two waveguide structures we discussed were applied to a basic waveguide in the evanescently coupled UTC-PDs. The entire structure of two types of the UTC-PDs to be designed was shown in **Fig. 3.13**. The structure horizontally consists of an input waveguide, an intermediate region and the UTC-PD on the waveguide. The input light from input waveguide is propagated to intermediate region, finally it is evanescently coupled to the upper side of the UTC-PD and absorbed into a very thin InGaAs absorption layer. The refractive index of the absorption layer should be designed higher than that of the other core layers because of photoabsorption. This is because the relation between the refractive index and the bandgap energy is generally inverse proportion [10]. Due to this relation, after being transparent at other core layers, the input light with the wavelength of 1.55 μm is absorbed at the absorption layer with high absorption coefficient α [11], which has the lowest bandgap energy with the highest refractive index at the waveguide structure. Furthermore, a matching layer which is located on the top of the waveguide guiding layer and under absorption layer was introduced. The matching layer is

used to improve photoabsorption by tuning the optical intensity and getting over the impedance mismatch between the optical guiding layer and the optical modes in the absorption layer [12-13]. Therefore, the matching layer can be one of the factors to be considered on the design of UTC-PD. To operate the device at high-frequency, the dimension of the UTC-PD and the thickness of the absorption layer should be considered carefully due to the tradeoff between bandwidth and quantum efficiency [14]. As for the performance of the device to be operated, it is available to obtain a higher quantum efficiency by a longer carrier transit time, whereas the time decreases the bandwidth.

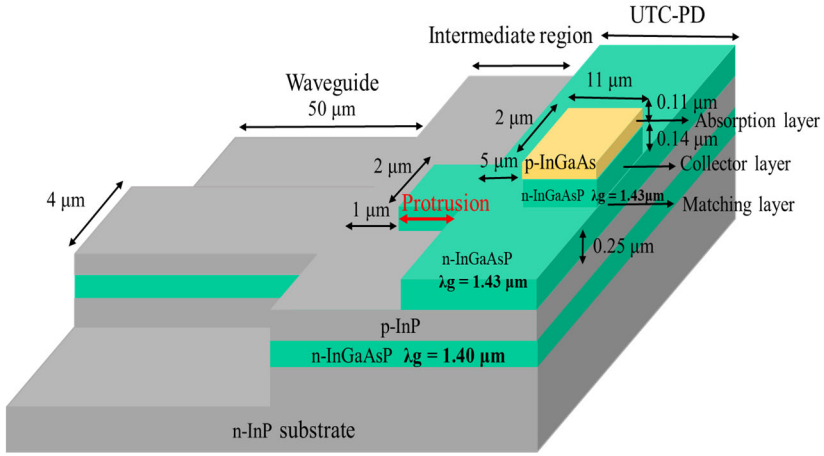

(a)

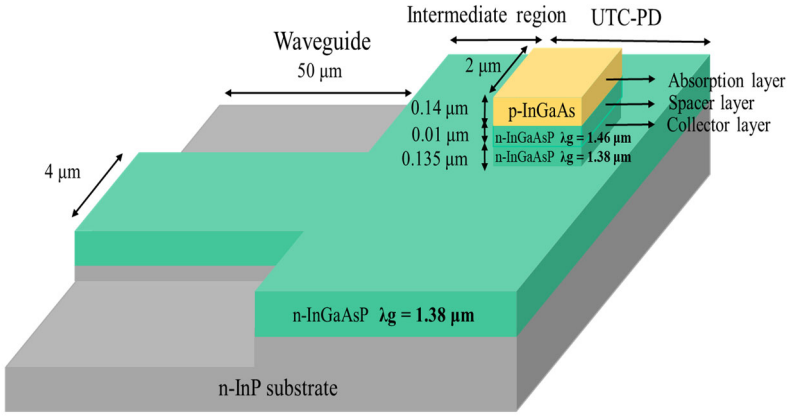

(b)

Fig. 3.13 Evanescently coupled UTC-PD. (a) 3- layered structure. (b) 2-layered structure.

Therefore, the proper range of dimension and the thickness of absorption layer is required according to the relation as shown in **Eqs. (3.4.1)-(3.4.2)**, each variable means that capacitance C, permittivity $\in_{\mathbf{0}}$, relative permittivity $\in_{\boldsymbol{r}}$, PD width W, PD length L, absorption layer thickness d, and resistance R, 3dB-RC frequency f_{CR}, respectively.

$$C = \in_{\mathbf{0}} \in_{\boldsymbol{r}} \frac{WL}{d} \tag{3.4.1}$$

$$f_{CR} = \frac{1}{2\pi CR} \tag{3.4.2}$$

In **Eq. (3.4.1)**, the absorption layer thickness of d should be large enough and both the width W and the length L should be reduced because the capacitance is required to be low for high-frequency operation. However, too large thickness of d causes longer carrier transit time which interrupts high-speed operation. The width W is also limited by optical coupling. Thus, the optimization of d and W and finding reduced length L are important to design the UTC-PD.

Firstly, the 3-layered waveguide integrated UTC-PD expressed as **Fig. 3.13 (a)** was designed for 11 μm-long and 2 μm-wide UTC-PD as extremely small area for high-frequency operation at 600 GHz according to the relation described in **Eqs. (3.4.1)-(3.4.2)**. The input waveguide which has cladding layer and core layer on the substrate is needed for coupling to the input light and guiding the light to the UTC-PD region. The UTC-PD has 4 μm-wide and 50 μm-long input waveguide with a certain amount of etching, also 1 μm-long space in the intermediate region and 5 μm-long space in UTC-PD region for better gradual guiding. The 4 μm-wide input waveguide with a large optical field leads to more focused coupling to the 2 μm-wide PD. At the matching layer, the protrusion length of the intermediate region with 2 μm-wide width before the 5 μm-long space should be considered because an appropriate protrusion length can obtain a higher quantum efficiency as dominant parameter [15]. **Figure**

3.14 shows the simulated result of the photoabsorption efficiency as a function of the protrusion length and the width of input waveguide. The result confirmed that the efficiency of 6 μm-long protrusion length was a maximum at 4 μm-wide input waveguide for 3-layered structure. Then, the 2-layered waveguide integrated UTC-PD was also designed to make 10 μm or 20 μm or 30 μm-long and 2 μm-wide UTC-PD for the 600 GHz operation. The UTC-PD as shown in **Fig. 3.13 (b)** has also the same 4 μm-wide and 50 μm-long input waveguide with an appropriate etching compared to 3-layered structure. The 5 μm-long intermediate region enables to get a progressive guiding of the light to the absorption layer. **Figure 3.15** shows that maximum efficiency of around 0.2 was obtained at 0.03 μm-thick matching layer and no matching layer also has the efficiency of near 0.2. Due to the simulated results, we chose no matching layer for the UTC-PD based on 2-layered structure. With two kinds of UTC-PDs mentioned above, we investigated each photoabsorption efficiency. According to used parameters in the bending efficiency calculation, the efficiency depending on the thickness both cladding layer and core layer were investigated.

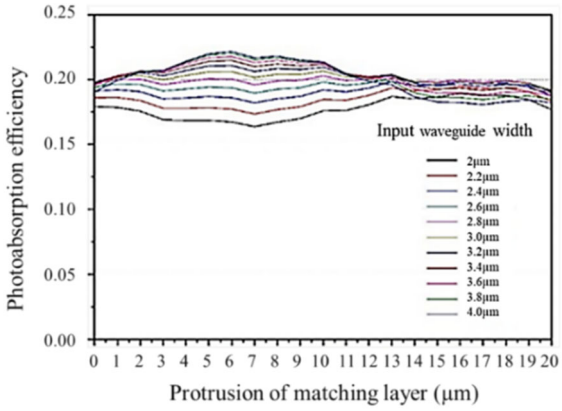

Fig. 3.14 Photoabsorption efficiency dependent on protrusion of matching layer and input waveguide width.

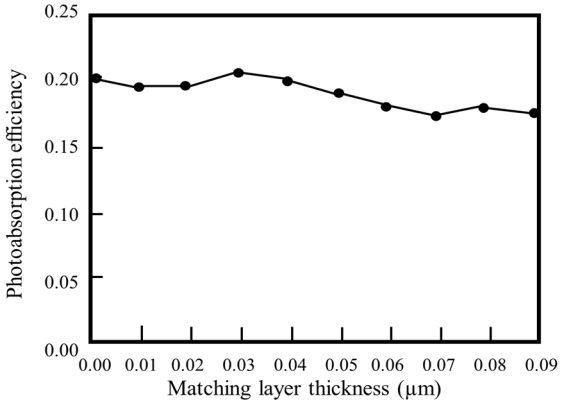

Fig. 3. 15 Efficiency as a function of matching layer thickness.

Figure 3.16 (a) shows that the photoabsorption efficiency of the 3-layered structure has the maximum of 0.23 at 0.2 μm-thick cladding layer which is the same as the best cladding layer thickness of the bending waveguide, whereas the efficiency of 0.22 was obtained at 0.1 μm-thick cladding layer in the chosen waveguide structure. **Figure 3.16 (b)** represents that the photoabsorption efficiency depending on core layer at the 2-layered structure has a maximum efficiency of 0.27 at 0.3 μm-thick core layer since less than 0.3 μm-thick core layer showed a lack of a single mode in the simulation.

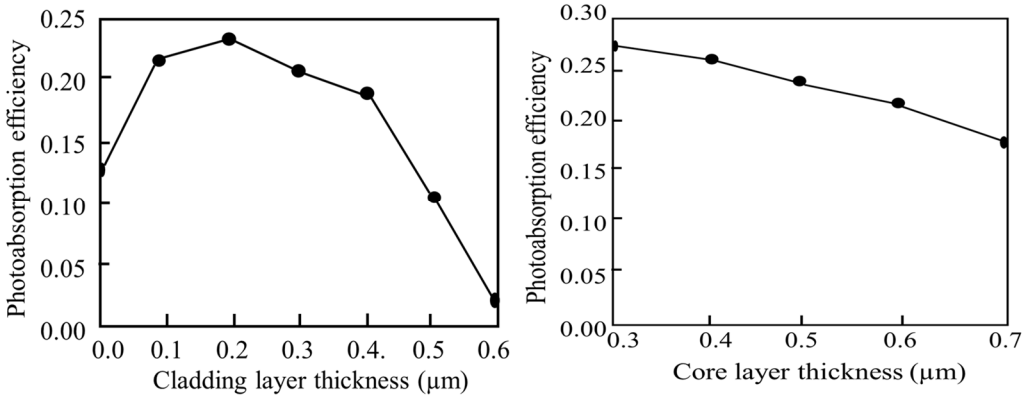

(a) (b)

Fig. 3.16 Photoabsorption efficiency. (a) 3-layered structure. (b) 2-layered structure.

The optical field distribution at both structures in **Fig. 3.17 (a)** shows that the guide light along input waveguide is evanescently coupled and absorbed into photoabsorption layer with the phenomenon of going up and down at the 3-layered structure because of a smaller photoabsorption while the 2-layered structure in **Fig. 3.17 (b)** shows a relatively simple distribution because of a larger photoabsorption.

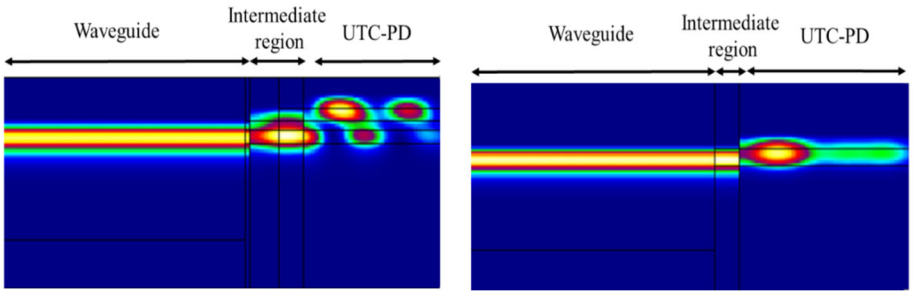

(a) (b)

Fig. 3.17 Optical field distribution at optimized structure. (a) 3-layered structure. (b) 2-layered structure.

Finally, we investigated each total efficiency to determine the final structure between the two UTC-PDs. The total efficiency η is calculated using the product between the bending efficiency estimated in Chapter 3.2 and the photoabsorption efficiency. The maximum of total efficiency of the 3-layered structure is approximately 0.22 at 0.2 μm-thick cladding layer as shown in **Fig. 3.18 (a)** even if the fixed cladding layer is 0.1 μm as we chose in Chapter 3.1. On the other hand, the total efficiency of the 2-layered structure as shown in **Fig. 3.18 (b)** indicates a maximum of 0.26 at 0.4 μm-thick core layer thickness instead of our fixed 0.5 μm-thick core layer in the Chapter 3.1. Based on the total efficiency, the $\eta_{2-\text{layered}}$ of 0.26 at 2-layered structure was higher than the $\eta_{3-\text{layered}}$ of 0.22 at 3-layered structure. We concluded that the 2-layered structure is more suitable for generation a higher THz-power and a device fabrication.

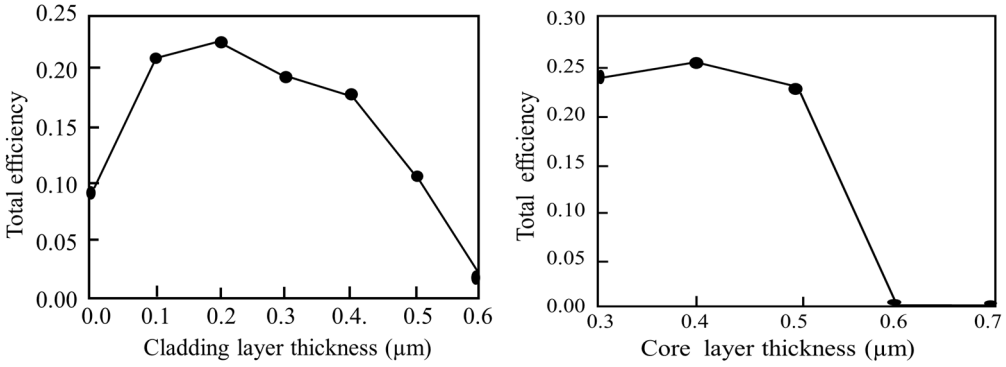

(a) (b)

Fig. 3.18 Total efficiency. (a) 3-layered structure. (b) 2-layered structure.

Consequently, an achievable photocurrent or optical power in terms of device performance was also calculated using $\eta_{2-\text{layered}}$ of 0.26 at the 2-layered structure at 1.55 μm wavelength**.** **Equation (3.4.3)** describes an expected photocurrent at the fabricated device. Each variable means that output photocurrent *I*, Plank constant $h = 6.63 \times 10^{-34}$ J · s, the speed of light $c = 3 \times 10^{8}$ m/s, and electric charge $e = 1.602 \times 10^{-19}$ C, respectively. The calculated photocurrent using **Eq. (3.4.3)** proved that this device can make 0.32 mA output photocurrent per 1mW optical input power. Thus, the expected responsivity at chosen structure was confirmed as 0.32 A/W while that of about 0.27A/W was obtained at 3-layered structure.

$$I = \eta \frac{\lambda e}{hc} \text{ [mA]} \qquad \textbf{(3.4.3)}$$

3.5 Performance of arrayed photomixers

Based on the simulated results of each component, we fabricated the photomixer chip with 3-layered structure as well as that with 2-layered structure even though the chosen structure is 2-layered structure. The whole structure of each fabricated devices is shown in **Fig. 3.19**. In

the fabricated devices, firstly, the two optical waveguides of 2- and 3-layered structure chosen in Chapter 3.1 were used as basic waveguide structure for making each component such as the bending waveguide, the MMI splitter, and the evanescently coupled UTC-PD in the photomixer chip. Secondly, the designed bending waveguides in Chapter 3.2 were used at the corner of each optical path, and they were located at between the 1x2 MMI splitter outputs and each UTC-PD for optical power feeding. Thirdly, designed six 1x2 MMI splitters were applied to a power divider which distributes the six guided optical powers equally to twelve evanescently coupled UTC-PDs simulated in Chapter 3.4. Finally, antennas were integrated with the UTC-PDs.

At the photomixer chip as shown in **Fig. 3. 19 (a)**, the input lightwaves from an edge of the device are guided along optical waveguides, amplified by the SOAs, passed by phase shifters and distributed through feeding waveguides, divided by 1x2 MMI splitters and introduced into the UTC-PDs while the photomixer chip in **Fig. 3.19 (b)** has the same configuration except SOAs. A slot antenna is connected to the UTC-PD, which radiates a terahertz wave into the air. The integrated device is designed for generating 600-GHz wave from two lightwaves whose optical frequency difference is 600 GHz.

In this preliminary experiment, we measured to testify just its optical-to-electrical conversion using a single wavelength of 1.55 μm without using SOAs and phase shifters. A continuous lightwave of 1.55 μm wavelength is generated from a laser diode. Then, it is amplified by an erbium–doped fiber amplifier (EDFA) and edge-coupled into input waveguide of the device. Inside the device, the lightwave passes through the feeding waveguide. Finally, it is evanescently coupled and detected at the UTC-PD.

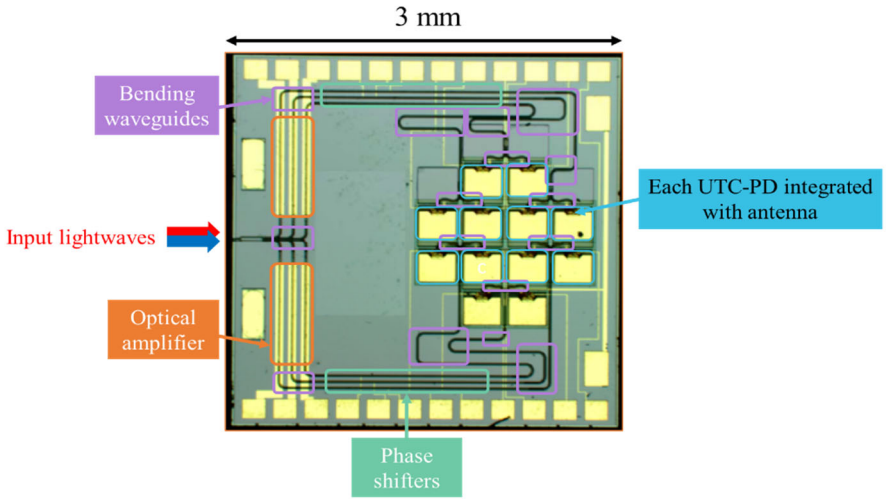

(a)

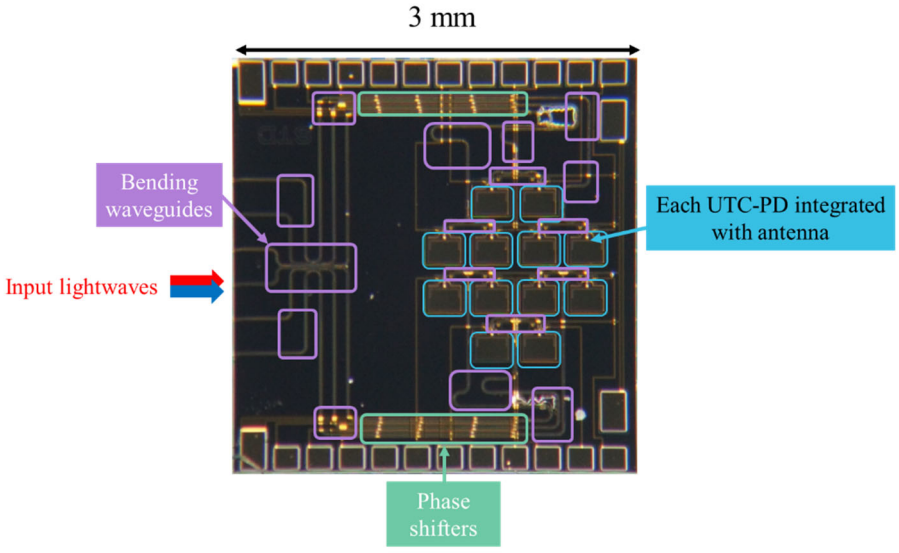

(b)

Fig. 3.19 Photograph of fabricated arrayed photomixers. (a) 3-layered structure. (b) 2-layered structure.

At first, we measured the photomixer device based on 3-layered structure. We measured the dark current of the UTC-PD to be 0.017 mA without an amplification of SOA. Then, we increased the optical input power by amplifying at the EDFA. **Figure 3.20 (a)** shows the measured net photocurrent as a function of optical input power at the device of the 3-layered structure. We obtained 0.0135 mA of net photocurrent at the optical input power of 152.6 mW.

The responsivity of the device is about 0.09 mA/W.

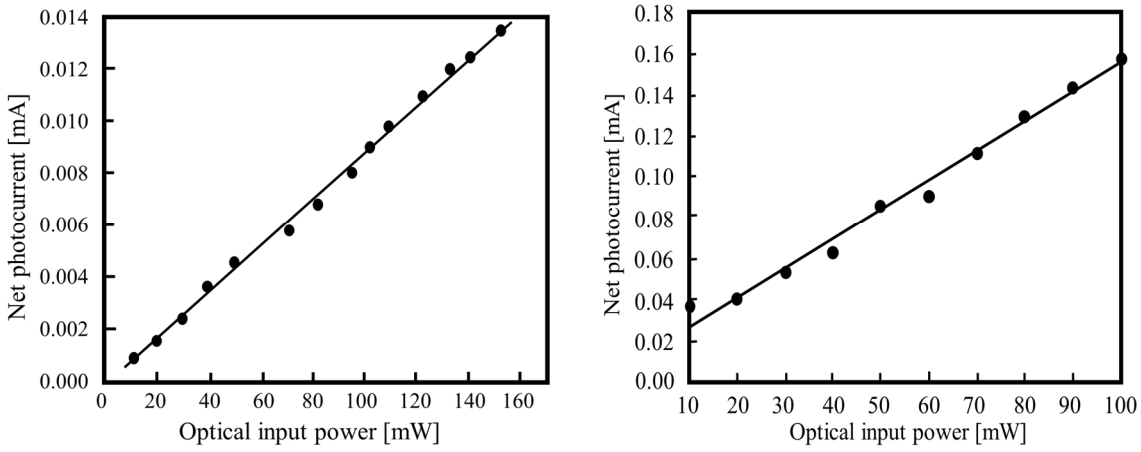

(a) (b)

Fig. 3.20 Net photocurrent as a function of optical input power (a) 3-layered structure (b) 2-layered structure.

Secondly, in the same way, the net photocurrent depending on the optical input power was measured at the device of the 2-layered structure. The measured dark current was 0.0107 mA. The net photocurrent of 0.1593 mA was achieved at optical input power of 100 mW. This result indicates that the responsivity is nearly 1.6 mA/W. Even though the efficiency at the result of 3-layered structure is small due to the large attenuation at the SOA, it is proportional to the input power, which indicates successful optical-to-electrical conversion at the integrated device. Likewise, the efficiency of fabricated photomixer based on the 2-layered structure is low, but the responsivity of 2-layered structure is higher than that of 3-layer structure as we expected in the simulated results. The expected performance by the simulation results does not correspond to the responsivity of the fabricated UTC-PDs. This is because there was difficulty in the optical coupling between an optical fiber and the photomixer chip.

3.6 Conclusions

In Chapter 3, two types of photomixers based on the two different waveguide structures were investigated by one-dimensional and three-dimensional simulation. Each component of the basic waveguide, the MMI, the bending waveguide and the evanescently coupled UTC-PD was designed. Finally, the performance of the fabricated photomixers was measured.

Firstly, in Chapter 3.1, the confinement factor at the under mesa to estimate the amount of radiation to the under mesa was simulated using each etching depth and five kinds of core layers. We obtained the two waveguides of 0.28 μm-thick core with 0.1 μm-thick cladding and 0.5 μm-thick with no cladding. Assuming that these two waveguides can be the base to design the photomixer structure, the optimized structures of the bending waveguide, the MMI and the evanescently coupled UTC-PD were investigated by three-dimensional simulation. The results of bending waveguide and MMI showed that the 3-layered structure is more sensitive to etching depth compared with 2-layered structure. With the result of the evanescently coupled UTC-PDs, the total efficiency was calculated to determine for the entire device fabrication. As a result, we fabricated a real device using 0.5 μm-thick core in the fabrication process even though we chose the 2-layered structure of 0.4 μm-thick core with no cladding. Then, the efficiency of the two fabricated integrated devices was measured for preliminary test. We confirmed that 0.0135 mA of net photocurrent at 152.6 mW of optical input power at the 3-layered structure while 0.1593 mA of net photocurrent at the 2-layered structure was obtained at optical input of 100 mW. Thus, we confirmed that the responsivity of the 2-layered structure was higher than that of the 3-layered structure as we expected in the design of the photomixers. The results indicate successful optical-to-electrical conversion thought it shows a low efficiency by a weak coupling between the optical fiber and the photomixer chip.

References

[1] T. Ishibashi, T. Furuta, H. Fushimi, S. Kodama, H. Ito, T. Nagatsuma, N. Shimizu, and Y. Miyamoto, "InP/ InGaAs uni-traveling-carrier photodiodes," IEICE Trans. Electron, vol. E83-C, no. 6, pp. 938-949, Jun. 2000.

[2] B. Broberg and S. Lindgren, "Refractive index of $In_{1-x}Ga_xAs_yP_{1-y}$ layers and InP in the transparent wavelength region," J.Appl. Phys, vol.55, no.9, May. 1994.

[3] K. Okamoto, "Fundamental of optical waveguides," Second edition, Academic Press, New York, Chap 1, 2006.

[4] A. Melloni, F. Carniel, R.Costa, and M. Martinelli, "Determination of bend mode characteristics in dielectric waveguides," J. Light. Technol, vol. 19. no. 4, Apr. 2001.

[5] T. Hirono, M. Kohtoku, Y. Yoshikuni, W. W. Lui, and K. Yokoyama, "Optimized offset to eliminate first-order mode Excitation at the junction of straight and curved Multimode Waveguides," IEEE Photonics technology letters, vol. 10, no. 7, Jul. 1998.

[6] A. Melloni, P. Monguzzi, R. Costa, and M. Martinelli, "Design of curved waveguides: the matched bend," J. Opt. Soc. Am. A/vol. 20, no. 1, Jan. 2003.

[7] E.-G. Neumann, "Curved dielectric optical waveguides with reduced transition losses," Proc. Inst. Elect. Eng., pt. H, vol. 129, pp. 278–280, 1982.

[8] S.-P. Chen and H.-G. Unger, "Low loss bends for planar optical waveguide," AEÜ Band 42. Heft 4, pp. 256-259, 1988.

[9] M. Błahut and A. Opilski, "Multimode interference structures-new way of passive elements technology for photonics," Opto-Electron, Rev., vol.9, no. 3, pp. 293-300, 2001.

[10] T. S. Moss, "Relations between the Refractive Index and Energy Gap of Semiconductors," Phys. Stat. Sol. (b) 131, 415, 1985.

[11] E. D. Palik, "Handbook of Optical Constants of Solids," Academic Press NY, 1985.

[12] R. J. Deri and O. Wada, “Impedance matching for enhanced waveguide/photodetector integration,” Appl. Phys. Lett, vol. 55, pp. 2712-2714, Dec.1989.

[13] A. Beling, H.-G. Bach, G. G. Mekonnen, R. Kunkel and D. Schmidt, “Miniaturized waveguide-integrated p-i-n photodetector with 120-GHz bandwidth and high responsivity,” IEEE Photonics technology letters, vol. 17, no.10, Oct. 2005.

[14] K. Kato, “Ultrawide-Band/High-Frequency Photodetectors,” IEEE Trans. Microw. Theory Tech, vol. 47, no. 7, Jul. 1999.

[15] L. Giraudet, F. Bandfi, S. Demiguel, and G.Hervé-Gruyer, “Optical Design of Evanescently Coupled, Waveguide-Fed Photodiodes for Ultrawide-Band Applications,” IEEE, Photonics technology letters, vol.11, no.1, Jan. 1999.

4. Arrayed light sources

4.1 Design of multimode interference splitter and bending waveguide

With design of the arrayed photomixers, the light sources which have the same number of arrays to provide same sets of dual wavelengths that can generate terahertz carrier frequency through optical coupling to the arrayed photomixers were considered. Furthermore, for compactness without fiber-optic configuration, we suggested the light sources realized by monolithic integration, which consist of several optical components such as lasers, the MMIs and the SOAs in a single chip. In terms of this kind of monolithic integration with the dual-mode lasers, the integrated devices using distributed feedback lasers (DFB-LDs) [1-2] and distributed bragg reflector lasers (DBR-LDs) [3] have been reported with the merits of wide frequency tuning range and compactness. We made the number between two devices to be the same because each SOA output is optically coupled to each input of arrayed UTC-PDs one by one. Thus, the number of UTC-PDs at the integrated chip corresponds to the number of SOA outputs at the arrayed light sources.

We designed two types of arrayed light sources such as 8- and 12-arrayed light sources, respectively for realization of 8- and -12 arrays at the proposed THz-wave generator module. The arrayed light sources have three components of two DFB-LDs, the MMIs as couplers and splitters, and the SOAs for amplifying the optical power. The DFB-LDs were located side-by-side. Because the merit of this placement which provides a stability to have same condition at the two lasers has been reported [4]. The DFB-LDs have a heterostructure with a bragg grating near active region and a single longitudinal mode in the output, and widely used as light source for signal transmission in optical communication system [5]. The MMIs are used to couple and

split a single mode lightwaves. Thus, the MMIs are designed for making optical coupler of coupling two lightwaves from the lasers. They also function as power divider into each SOA output to provide the same power with each arrayed UTC-PDs. Finally, the SOA amplifies the optical power at each MMI output. In order to design the integrated light sources, the cross-sectional structure used at the two light sources consists of an InGaAsP core with bandgap wavelength of 1.3 μm and another InGaAsP core with bandgap wavelength of 1.1 μm surrounded by InP cladding layer, which is buried waveguide structure as shown in **Fig. 4.1 (a)**. First of all, the 1x2 MMI design is needed to construct power divider as 1x2 MMI splitter and its design is equally applied to 2x1 MMI coupler. The simulated structure of the 1x2 MMI is shown in **Fig. 4.1 (b)**. The MMI has an input and two outputs with 1.6 μm width. The width and length of the MMI must be optimized for optical power splitting.

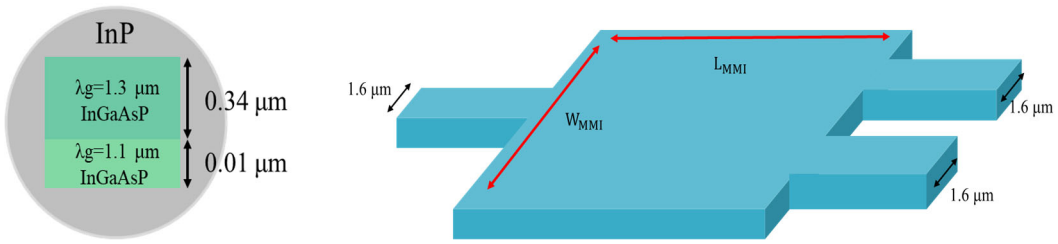

(a) (b)

Fig. 4.1 Simulated structure. (a) Layered waveguide structure. (b) 1x2 MMI structure.

In the simulated result of the 1x2 MMI in **Fig. 4.2 (a)**, at each output, the maximum output power reaches nearly 0.48 at an optimized MMI length of 52 μm length with 1.7 μm spacing between two MMI outputs. The simulated result as shown in **Fig. 4.2 (b)** represents equally distributed power at the outputs and stable optical field distributions.

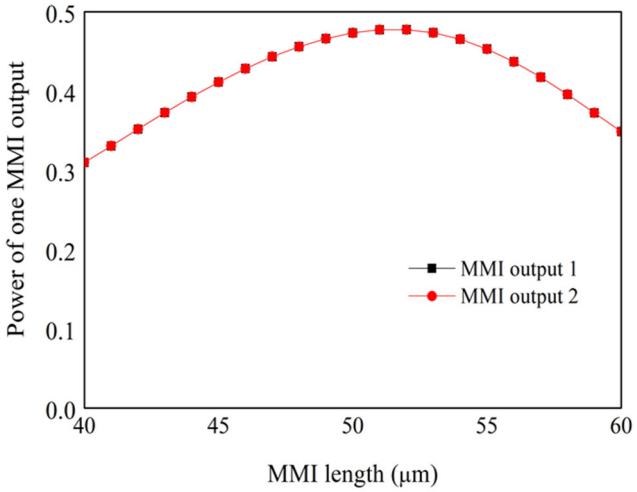

(a)

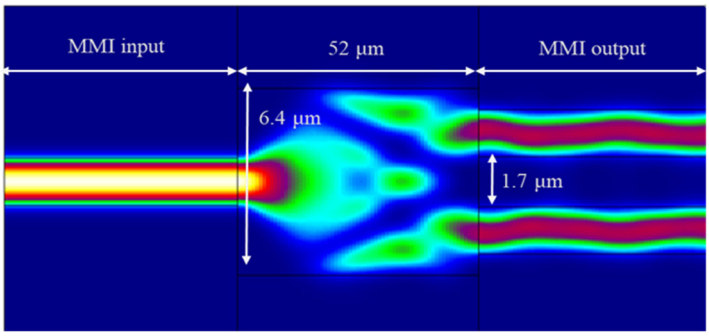

(b)

Fig. 4.2 Simulated results of 1x2 MMI. (a) Each output power. (b) Optical power distribution.

Based on this result, we designed some power splitting parts at the 8- and 12-arrayed light sources which can be used as light sources in combination with 8-arrayed photomixers and 12-arrayed photomixers. The 8-arrayed light sources shown in **Fig. 4.3** are designed by the simulated result of the 1x2 MMI. The integrated device consists of two DFB-LDs, the MMIs and eight SOAs. The lightwaves from DFB-LDs are coupled at 2x1 MMI coupler which is designed by the same structure of 1x2 MMI splitter. And the coupled lightwaves are divided through seven cascaded 1x2 MMI splitters. The cascaded structure is expected to have more

uniformly split powers because of its symmetric structure compared to a 1x8 MMI splitters [6] and finally amplified at the SOA. The lightwaves are amplified by the SOAs which are aligned with 250 μm pitch. A 250 μm-pitch micro-lens array (MLA) is attached at the output of the SOAs.

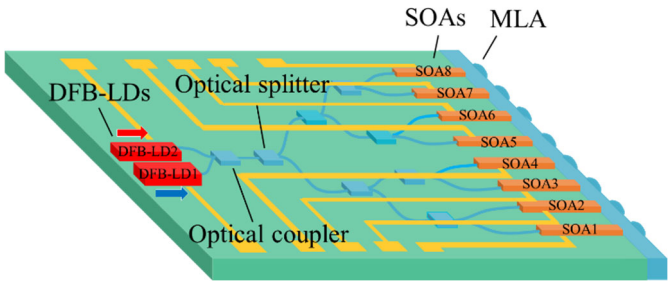

Fig. 4.3 Structure of 8-arrayed light sources.

For the 12-arrayed light sources, the 1x12 MMI splitters to make twelve SOA outputs are designed with 2x1MMI coupler design. We investigated the optimized length at the fixed width of 47.2 μm which was optimized for the 1.6 μm-wide 1x12 MMI input and outputs. The simulated results of the output power at each MMI output are shown in **Fig 4.4**. The 12-arrayed light sources were optimized at the MMI with a length of 407.5 μm and a width of 47.2 μm even with a power variation of ± 5 %.

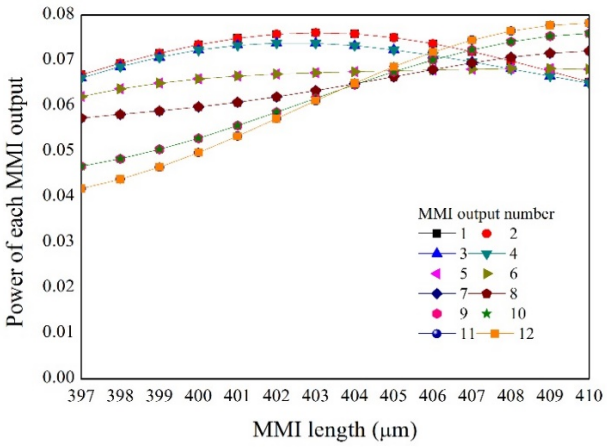

Fig. 4.4 Simulated output power as a function of MMI length.

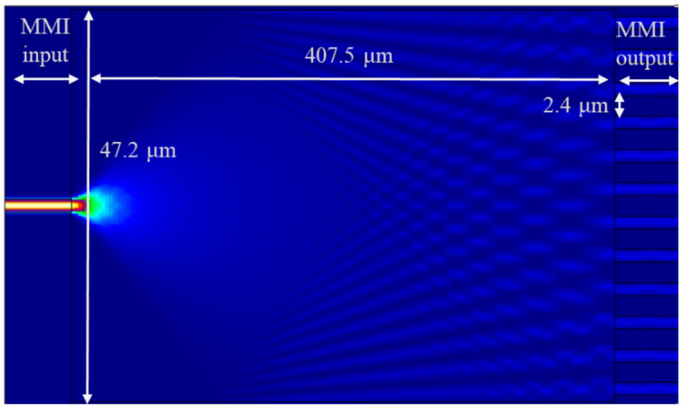

Fig. 4.5 Simulated power distribution of 1x12 MMI.

Figure 4.5 shows the power distribution of the 1x12 MMI. The power from the input is equally distributed into each output.

The bending waveguide is used to match optical path length with same phase. We simulated bending loss to find the optimized bending radius with low loss. We aimed to apply the optimized result of the bending waveguide to both 8- and 12- arrayed light sources. The bending waveguide is used at the input of 2x1 MMI coupler, the output of 1x2 MMI splitter and 1x12 MMI splitter. **Figure 4.6 (a)** shows the configuration of the bending waveguide and the simulated result bending waveguide in **Fig. 4.6 (b)**. The bending waveguide has 1.6um width and a radius of r with 90 degree curvature. The result indicates that the bending loss decreases with increase at bending radius. The 0.07 dB of bending loss at 200 μm bending radius was obtained. In the simulated result, the bending loss was remarkably reduced from the radius of 200 μm and more than 200 μm curvature is needed to connect from each output of 1x12 MMI to each SOA. Consequently, we chose more than 200 μm radius to make each bending waveguide for the MMIs and especially, gradual bending waveguide using each different radius for 1x12 MMI splitter.

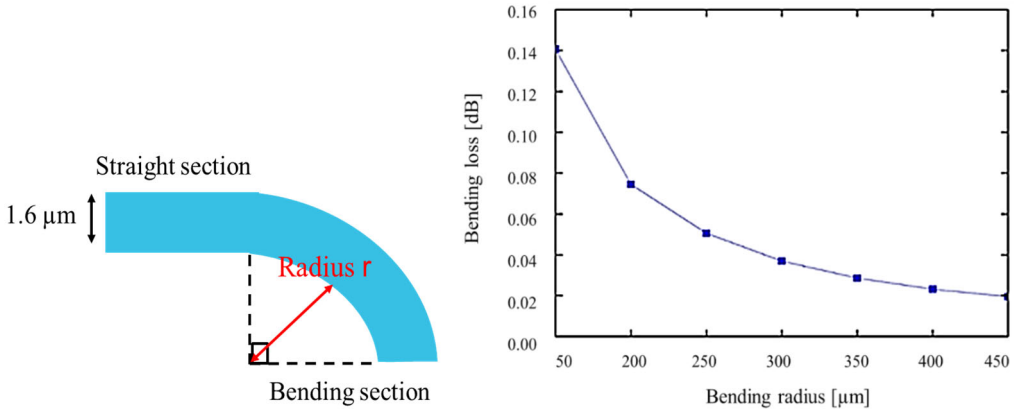

(a) (b)

Fig. 4.6 Bending waveguide. (a) Simulation model of bending waveguide. (b) Bending loss a function of bending radius.

The 12-arrayed light sources shown in **Fig. 4.7** are fabricated based on the simulated result of the 1x12 MMI and the bending waveguide. The integrated device consists of two DFB-LDs, the MMIs and twelve SOAs. The lightwaves from the DFB-LDs are coupled by 2x1 MMI coupler and the coupled lightwaves are distributed through 1x12 MMI splitter. Finally, they are amplified at the SOA. The SOA outputs of 12-arrayed light sources are also aligned with 250 μm-pitch with attached 250 μm-pitch MLA. The integrated chips both 8- and 12- arrayed light sources were sited on an alumina-based wiring board, which was mounted on a metal package via a Peltier cooler.

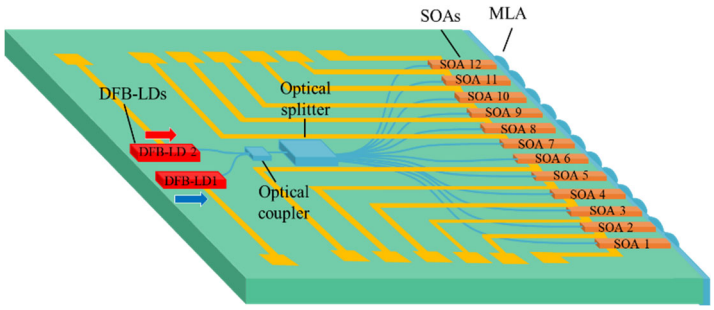

Fig. 4.7 Schematic of 12-arrayed light sources.

4.2 Performance of arrayed light sources

Based on the simulated results of bending waveguide,1x2 MMI splitter and 1x12 MMI splitter, we fabricated the two devices of 8- and 12 -arrayed light sources. **Figure 4.8** shows the fabricated devices.

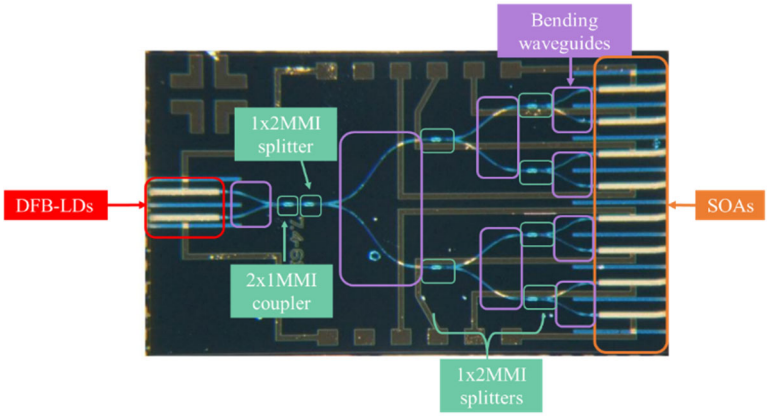

(a)

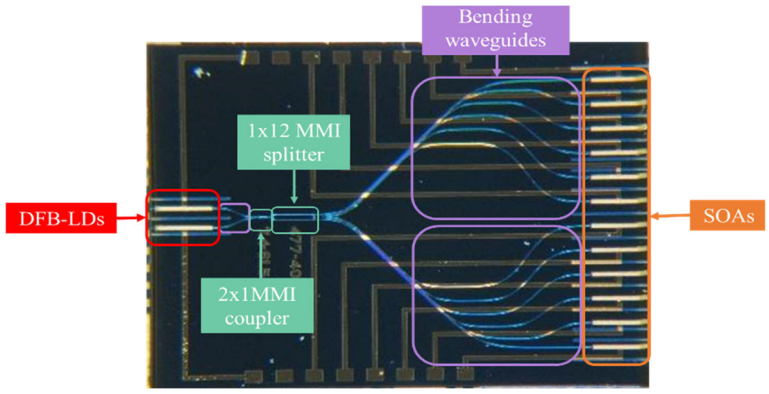

(b)

Fig. 4.8 Photograph of fabricated light sources. (a) 8-arrayed light sources. (b)12-arrayed light sources.

In 8-arrayed light sources as shown in **Fig. 4.8 (a)**, designed 1x2 MMI was used at both 2x1 MMI coupler and 1x2 MMI splitters. The bending waveguide was located at the input of 2x1

MMI coupler and output of 1x2 MMI splitters. **Figure 4.8 (b)** shows the fabricated device of 12-arrayed light sources. The designed bending waveguide was used at the input of 2x1 MMI coupler and the output of 1x12 MMI splitter for gradually increasing bending structure with various radius more than 200 μm. The designed 1x12 MMI splitter was located to make the twelve SOAs. With the fabricated the two light sources, 8- and 12-arrayed light sources, their performance was measured to confirm optical spectrum and output power characteristic. **Figure 4.9** shows the experimental setup of the measurement. In this experiment, the micro lensed fiber was used for optical coupling to check the optical power at each SOA output. We observed the change in the output power at power meter with increasing each SOA current. At first, the optical spectrum at both light sources, which has two wavelengths from two DFB-LDs was clearly confirmed at the SOA current of 50 mA and DFB-LDs current of 50 mA through optical spectrum analyzer (OSA).

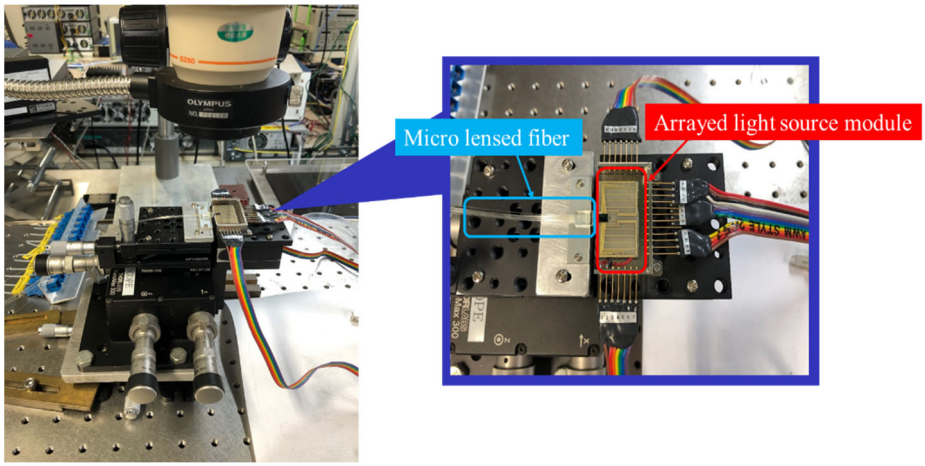

Fig. 4.9 Experimental setup for measuring output lights at fabricated arrayed light sources.

Figure 4.10 shows the measured results which indicate that the two light sources have wavelength difference of 4.67 nm with frequency difference of 593 GHz as approximately 600 GHz. The result confirmed that 600 GHz-wave generation by photomixing using the light sources is available. And then, the output power at each SOA output was observed. We measured the output power as a function of SOA current at both types of light sources with a fixed DFB-LDs current of 50 mA. **Figure 4.11 (a)** shows the output power of 8-arrayed light sources has a high uniformity within ± 1 % as expected from the simulated results.

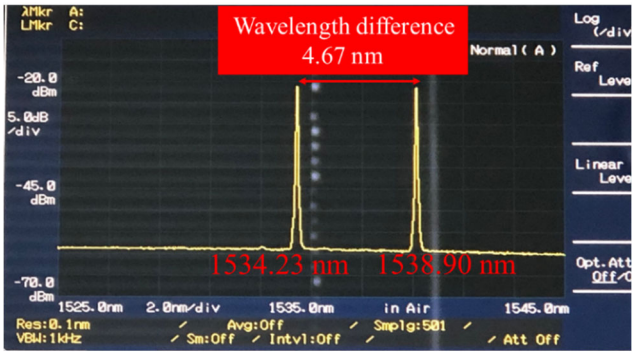

Fig. 4.10 Observed optical spectrum with two wavelengths of 1534.23 nm and 1538.90 nm.

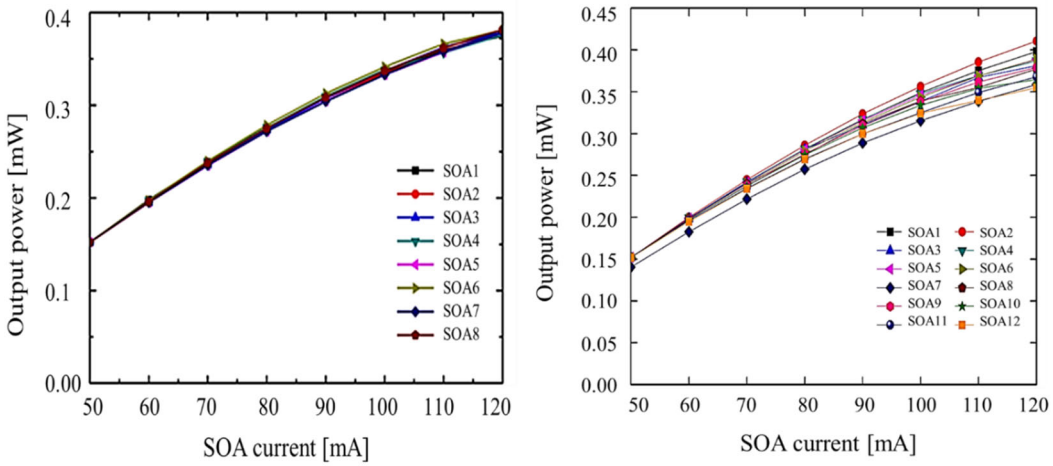

(a) (b)

Fig. 4.11 Measured output power as a function of SOA current. (a) 8-arrayed light sources. (b) 12-arrayed light sources.

Meanwhile, that of the 12-arrayed light source as shown in **Fig. 4.11 (b)** has some variation, but a uniform power would be obtained by tuning each SOA current. All the devices have a high power uniformity. They have a high uniformity within a difference of about 2%. Here, the measured value includes a low optical coupling efficiency with the fiber.

4.3 Conclusions

In Chapter 4, the design of the arrayed light sources consisting of two DFB-LDs, the MMIs and the SOAs was introduced. First of all, we designed 1x2 MMI for making both 8- and 12- arrayed light sources. Then, 1x12 MMI for 12-arrayed light sources was simulated. Based on the optimized results of the MMIs, we fabricated the two types of integrated devices. The stable dual wavelengths of the light sources were observed at the optical spectrum. Then, we measured the light power of each SOA output using the two devices. The 8-arrayed light sources have a higher power uniformity compared to 12-arrayed light sources even though the measured output power shows high power uniformity at both cases. From all the results, we confirmed that the arrayed light sources can be applicable to the proposed terahertz wave generator.

References

[1] N. Kim, J. Shin, E. Sim, C.W. Lee, D.-S. Yee, M.Y. Jeon, M. Jang, and K.H. Park, "Monolithic dual-mode distributed feedback semiconductor laser for tunable continuous wave terahertz generation," Opt. Express, vol. 17, no. 16, Aug. 2009.

[2] F. van Dijk, G. Kervella, M. Lamponi, M. Chtioui, F. Lelarge, E. Vinet, Y. Robert, M.J. Fice, C.C. Renaud, A. Jimenez, and G. Carpintero, "Integrated InP Heterodyne Millimeter Wave Transmitter," IEEE Photon. Technol. Lett, vol.26, no.10, pp.965–968, 2014.

[3] G. Carpintero, S. Hisatake, D. Felipe, R. Guzman, T. Nagatsuma, and N. Keil, "Wireless Data Transmission at Terahertz Carrier Waves Generated from a Hybrid InP-Polymer Dual Tunable DBR Laser Photonic Integrated Circuit," Sci. Rep. 8 (1), 3018, 2018.

[4] E. García-Muñoz, K. A. Abdalmalak, G. Santamaría, A. Rivera-Lavado, D. Segovia-Vargas, P. Castillo-Araníbar, F. Van Dijk, T. Nagatsuma, E.R Brown, R.C Guzman, H. Lamela, and G. Carpintero, "Photonic-based integrated sources and antenna arrays for broadband wireless links in terahertz communications," Semicond. Sci. Technol, 34 (2019) 054001 (8pp).

[5] G. Morthier and P. Vankwikelberge, "Handbook of Distributed Feedback Laser Diodes," Arctech House, Norwood, MA, 1997.

[6] Q. Chen, Q. Lu, and W. Guo, "Theory and simulation of multi-channel interference (MCI) widely tunable lasers," Opt, Express,vol. 23, no. 14, 13, Jul. 2015.

5. Demonstration of terahertz wave generation

5.1 Experimental configuration for terahertz power detection

Based on the measured results to confirm the performance of the fabricated integrated devices, we made an experiment for terahertz wave generation using the devices. But we used the arrayed UTC-PDs which has a bowtie antenna at each UTC-PD [1-2] as photomixers with a higher responsivity for a better coupling between the output of the light sources and the input of integrated UTC-PD chip. The integration between antennas and UTC-PDs for terahertz wave generation has been developed to get a better performance [3]. **Figure 5.1** shows the structure of the arrayed UTC-PD with bowtie antenna used at the experiment. The four bow-tie antennas were arrayed with a spacing of 500 μm.

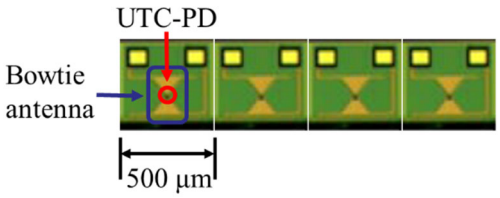

Fig. 5.1. Structure of bowtie antenna chip.

The 8-arrayed light sources for providing two lightwaves were chosen with respect to measured power uniformity compared to 12-arrayed light sources. Because it showed a high uniformity of ± 1 % at each SOA output as increasing SOA current in the previous experiment. And then, we set an experimental configuration for terahertz power detection and the mechanism of the terahertz wave radiation at the UTC-PD is shown in **Fig. 5.2.** As shown in **Fig. 5.2 (a)**, every two outputs of the light sources are optically coupled to the UTC-PD. A current injected into one of the DFB-LDs was modulated at 1kHz for a lock-in detection.

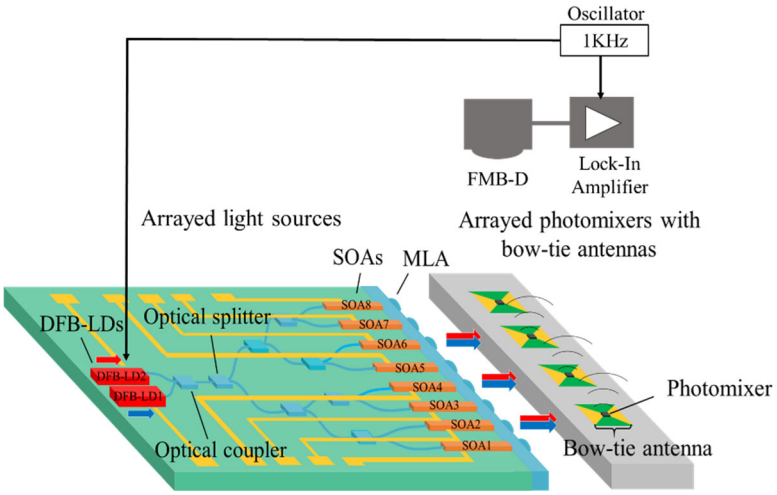

(a)

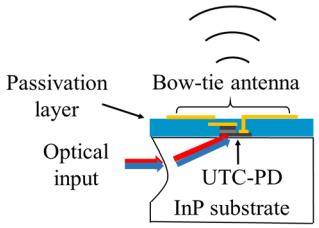

(b)

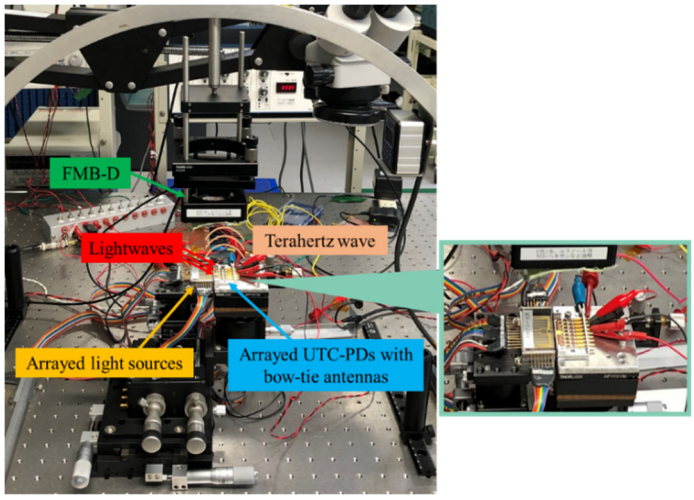

(c)

Fig.5.2. Experimental configuration. (a) Schematic of experimental setup. (b) Cross-sectional view at THz-wave generation at the bow-tie antenna. (c) Photograph of experimental setup.

The fermi-level managed barrier diode (FMB-D) was used due to a higher sensitivity compared with Schottky barrier diode (SBD) which is generally used as terahertz wave detector [4]. The FMB-D was located at a distance of 30 mm from the bow-tie antennas. The output voltage of the FMB-D was measured at the lock-in amplifier (LIA) which is used for detection of very small signal. The input lightwaves are refracted at the edge of the chip as shown in **Fig. 5.2 (b)** and introduced into each arrayed UTC-PDs with the 500 μm spacing, and terahertz wave is radiated through bow-tie antenna. **Figure 5.2 (c)** shows that the arrayed light sources and the arrayed UTC-PDs were aligned on an optical alignment stage. Every two outputs of arrayed light sources were matched with the three arrayed UTC-PD by the 500 μm spacing.

5.2 Beamforming at 600 GHz using integrated devices

Via the optical alignment of coupling between the light sources and the photomixers, we made an experiment for measuring an angular distribution of the terahertz wave. We rotated the FMB-D around the arrayed UTC-PDs in a plane parallel to the array direction from -20 to +20 degrees in the vertical direction. We measured the combined terahertz power at both two UTC-PDs and three UTC-PDs in the array as well as that of single UTC-PD as a reference. **Figure 5.3** shows the measured angular distribution of the generated terahertz power as a function of the FMB-D angle at each number of channels. We confirmed that the combined power from the three UTC-PDs indicates sharp peak arise from directional gain by arrayed configuration. The directivity of the two arrays represents similar distribution to that of the three arrays whereas single UTC-PD has flat angular distribution.

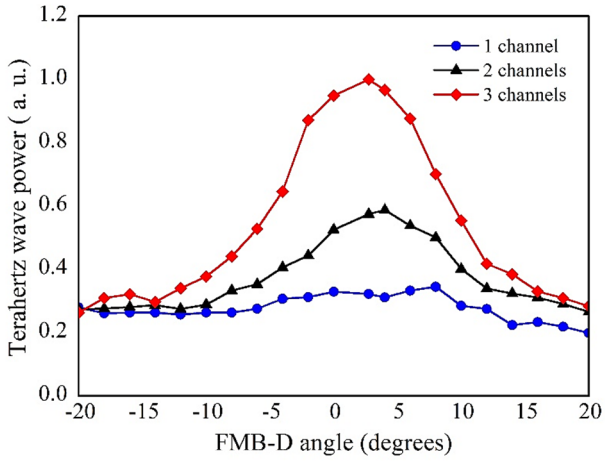

Fig. 5.3 Angular distribution of terahertz wave.

From the result of the combined terahertz power, the relation between the peak combined power and the number of channels is shown in **Fig. 5.4**. The measured peak power is superlinear with increasing the number of the channels. This analysis suggests the similar trend to the theoretical expectation that the generated THz power is proportional to the square of the number of channels in the relation according to $P = |N|^2|E|^2$ expressed in **Eq. (2.4.11)**.

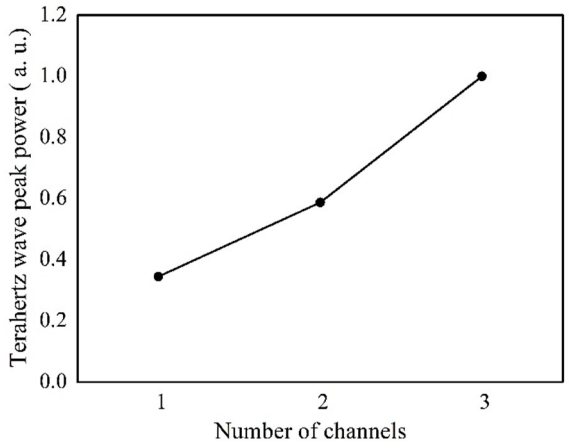

Fig. 5.4 Relation between combined peak power and number of channels.

5.3 Conclusions

In Chapter 5, the 600 GHz-wave beam forming using the light sources in combination with the arrayed photomixers was demonstrated. We confirmed that the combined terahertz power showed sharp peak from directional gain by array factor. From these results, the proposed module which consists of the arrayed light sources and the arrayed photomixers can be used for terahertz wave generator. The module has a potential to attain a beam steering by integrating the component of phase shifter in the near future.

References

[1] Y. Zhou, N. Nishiyama, H. Ito, T. Ishibashi, and K. Kato, “700 GHz terahertz wave beam combination by optical phase control,” Jpn. J. App. Phys. 58, SJJE03, 2019.

[2] Y. Zhou, G. Sakano, Y. Yamanaka, H. Ito, T. Ishibashi, and K. Kato, “600-GHz-Wave Beam steering by Terahertz-Wave Combiner,” Optical Fiber Communication Conference (OFC), M4J.1, 2018.

[3] C.C. Renaud, M. Natrella, C. Graham, J. Seddon, F. Van Dijk, and A. J. Seeds, “Antenna Integrated THz Uni-Traveling Carrier Photodiodes,” IEEE Journal of selective topics in quantum electronics, vol. 24, no. 2, Mar/Apr. 2018.

[4] H. Ito and T. Ishibashi, “InP/InGaAs Fermi-level managed barrier diode for broadband and low-noise terahertz-wave detection,” Jpn. J. Appl. Phys. 56 014101, 2017.

6. Conclusion and Outlook

6.1 Conclusion

Terahertz wave has been a promising frequency band for higher data rate wireless communication. Photonics-based method for the terahertz wave generation is realized specifically by photomixing technique, which uses two continuous lightwaves and optical-to-electrical conversion at high-speed photodiode as photomixer. In Chapter 1, the UTC-PD as photomixer for terahertz wave generation and the necessity of array configuration caused by power saturation at single UTC-PD were introduced. In addition to the photomixer arrays, the arrayed light sources which provide same sets of dual wavelengths to each array at the arrayed photomixers were suggested. Consequently, the development of the terahertz wave generator module consisting of the arrayed photomixers and the arrayed light sources was proposed. The two separate devices were designed based on optical waveguide structures using InP/InGaAsP material system. In Chapter 2, the principle of the optical waveguide, the MMI, the evanescent coupling structure, and the phased array antenna for design of our integrated devices was explained.

In Chapter 3, each component for arrayed photomixers was designed and the measured performance was described. Firstly, in Chapter 3.1, the confinement factor to the undermesa was investigated for finding basic waveguide structure to be used at our integrated devices. From the simulated results, the etching depth and the core layer thickness as dominant factors on the confinement factor were confirmed. Finally, the two eligible waveguide structures were chosen. They are 0.28 μm-thick core with 0.1 μm-thick cladding as 3-layered structure and 0.5 μm-thick with no cladding as 2-layered structure. Using the two waveguide structures, bending waveguides were investigated in Chapter 3.2. The optimization of bending radius, offset, and

the etching depth can be effective to get a higher bending efficiency. Each bending efficiency of 3- layered structure on cladding layer and that of 2-layered structure on core layer was calculated. The 1x2 MMI was optimized at the 6.5 μm width for 3- layered structure and 6.4 μm width for 2-layered structure though the two structures were optimized at 43 μm-long MMI. But the optimized structure at both waveguide structures showed a similarity by MMI properties. The dependency on etching depth at the 3-layered structure was higher than that of 2-layered structure. More than 1.9 μm etching for bending waveguide and 2.2 μm etching for MMI were required for the 3-layered structure. These results can be considered as correlation with waveguide simulation in Chapter 3.1. The confinement factor to the under mesa of 2-layered structure approached almost zero at a lower etching depth. Thus, the 2-layered structure has relatively less sensitive to the etching depth. Then, the features of the evanescently coupled UTC-PD was introduced in Chapter 3.4. To compare total efficiency between the two structures, each photoabsorption efficiency depending on the cladding layer at the 3-layered structure and the core layer at the 2-layered structure was investigated. Finally, the total efficiency which is defined as the product of the bending efficiency and the photoabsorption efficiency was calculated. The 3-layered structure was optimized at 0.28 μm-thick core layer with 0.2 μm-thick cladding layer while the fixed waveguide structure has 0.1 μm- thick cladding layer. The 2-layered structure was optimized at the 0.5 μm-thick core layer and no cladding layer. The total efficiency of the 2-layered structure was higher than that of the 3-layered structure ($\eta_{2-\text{ layered}} = 0.26 > \eta_{3-\text{layered}} = 0.22$). Consequently, the 2-layered structure enables to obtain the expected photocurrent nearly 0.32 mA which is applicable to provide a higher THz-power in the generation of 600 GHz-carrier frequency. We measured the efficiency at the two fabricated devices. In this experiment, we confirmed the responsivity of 0.09 mA/W at the 3-layered structure and 1.6 mA/W at 2-layered structure. The results indicate successful optical-

to-electrical conversion although a low efficiency was obtained by the difficulty on optical coupling between the optical fiber and the photomixer chip.

In Chapter 4, for providing the same sets of dual wavelengths with the photomixer arrays, the design of the arrayed light sources consisting of two DFB-LDs, the MMIs and the SOAs was introduced. The 8 - and 12-arrayed light sources were considered to match the number of photomixer array. Firstly, we designed 1x2 MMI for making both 8- and 12- arrayed light sources. The 1x2 MMI was optimized at 4 μm width and 52 μm length. Then, the 1x12 MMI for 12-arrayed light sources was simulated. The MMI was optimized at 407.5 μm length at 47.2 μm width. Based on the simulated results, we fabricated the two types of integrated devices. The stability of dual wavelengths produced at the light sources was observed at the optical spectrum. We measured the light power of each SOA output at the two light sources. The 8-arrayed light sources have a higher power uniformity compared to 12-arrayed light sources even though the measured output power shows a high power uniformity at both devices. We found that the light sources can be used as a part of the proposed THz-wave generator module.

In Chapter 5, the 600-GHz wave beam forming using the light sources in combination with the arrayed photomixers in the experiment was explained. We confirmed that the combined terahertz power indicates sharp peak from directional gain by array factor. From these results, the proposed module which consists of the arrayed light sources and the arrayed photomixers can be applicable to THz-wave generator.

To test the performance of the THz-wave generator preliminarily, we fabricated the prototype module of the generator being operated as a single module. The module consisting of the arrayed light sources and the arrayed UTC-PDs integrated antennas is shown in the following **Fig. 6.1** with the size of 59 mm length and 43 mm width. The module needs only

DC currents injected to the light sources as well as DC voltages applied to the UTC-PDs with the merit of a low complexity without using additional element for sources.

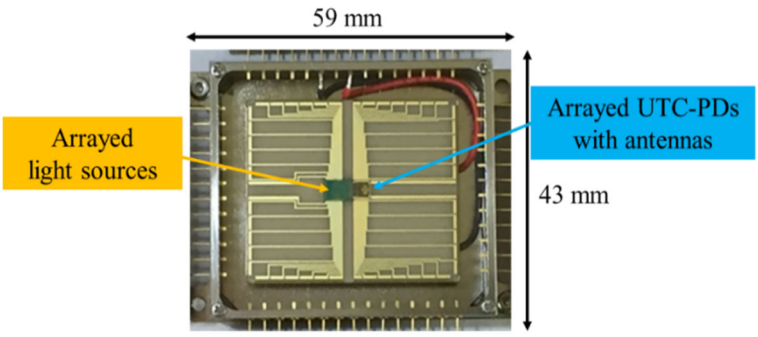

Fig. 6.1 Photograph of a prototype THz-wave generator module.

6.2 Outlook

In this research, the beam forming with a high directivity at the proposed THz-wave generator was demonstrated. In the near future, the beam steering for a flexible control of the radiated beam direction can be attained by integrating the component of a phase shifter. However, the problem of optical coupling between the arrayed light sources and the arrayed photomixers also should be improved for increased number of array element, which enables a higher THz power. With more advanced integration technology, the THz-wave generator can be applied to the wireless communication system.

List of abbreviations

UTC-PD	Uni-traveling carrier photodiode
RTD	Resonant tunneling diode
MMIC	Monolithic microwave integrated circuit
IMPATT	Impact ionization avalanche transit-time
TUNNETT	Tunneling transit-time
QCL	Quantum cascade laser
PIC	Phonic integrated circuit
EME	Eigen mode expansion
MMI	Multimode interference
VPD	Vertically illuminated photodetector
DFB-LD	Distributed feedback laser diode
DBR-LD	Distributed bragg reflector laser diode
SOA	Semiconductor optical amplifier
OSA	Optical spectrum analyzer
MLA	Micro lens array
EDFA	Erbium-doped fiber amplifier
FMB-D	Fermi-level managed barrier diode
SBD	Schottky barrier diode
LIA	Lock-in amplifier

Acknowledgement

I would like to express my sincere appreciation to Prof. Kazutoshi Kato who gave me a great opportunity to do the research of semiconductor photonics integrated device and always encouraged me to accomplish this research work patiently with unstinting advices. With this opportunity, I could further improve valuable insight concerning this research.

And I also would like to thank my thesis committee Prof. Haruichi Kanaya and Prof. Shunji Kimura for their thoughtful comments and suggestions about my thesis.

Secondly, I am really thankful to Assistant Prof. Takeshi Kuboki and my laboratory members who helped me when I faced difficulties on my research.

Finally, I would like to express my gratitude from deep in my heart to my family for support both materially and spiritually all the time.